Mischmetal substitution in $Nd_2Fe_{14}B$ sintered permanent magnets

by

Harika Chowdary Dasari

A thesis submitted to the graduate faculty

in partial fulfillment of the requirements for the degree of

MASTER OF SCIENCE

Major: Materials Science and Engineering

Program of Study Committee:
Jun Cui, Major Professor
Duane D Johnson
Matt J Kramer

The student author, whose presentation of the scholarship herein was approved by the program of study committee, is solely responsible for the content of this thesis. The Graduate College will ensure this thesis is globally accessible and will not permit alterations after a degree is conferred.

Iowa State University

Ames, Iowa

2023

TABLE OF CONTENTS

Page

LIST OF FIGURES

Page

LIST OF TABLES

Page

NOMENCLATURE

BSE	Back Scatter Electron
G/Gs	Gauss
Ha	Anisotropic Field
Hc	Coercivity
MM	Mischmetal
Ms	Saturation Magnetization
Oe	Oestered
REE	Rare-earth Elements
SEM	Scanning Electron Microscope

ACKNOWLEDGMENTS

This work was supported by the U.S. Department of Energy (DOE), Critical Materials Institute (CMI) at the Ames Laboratory under contract number DE-AC02-07CH11358. Ames Laboratory is operated for the DOE by Iowa State University. The document number assigned to this thesis/dissertation is IS-T 3342.

I would like to thank my committee chair, Prof. Jun Cui, and my committee members, Dr. Duane Johnson, and Dr. Matt Kramer, for their guidance and support throughout the course of this research.

In addition, I would also like to thank my friends, colleagues, the department faculty and staff for making my time at Iowa State University a wonderful experience. I want to also offer my appreciation to those who were willing to participate in my surveys and observations, without whom, this thesis would not have been possible.

ABSTRACT

Neodymium-iron-boron based permanent magnets are the preferred magnets for motor applications because of their high-energy production. However, the supply of neodymium is subject to high risks due to geopolitical and economical conflicts of interests. Cerium, lanthanum, and Mischmetal can be potential substitutes of neodymium as they have similar electronic structures as the neodymium, and more importantly, they are abundant and low-cost. One of the important properties of permanent magnets is coercivity, which defines the ability of the magnet to work in a demagnetization field. Coercivity depends on magneto crystalline anisotropy and microstructure. The microstructure at the grain boundaries in sintered 2:14:1 type magnet helps to remove defects and improve coercivity by reducing magnetostatic interactions between grains. Addition of nonmagnetic, low melting point alloys like PrCu to the magnetic material may prevent magnetic coupling of adjacent grains by forming continuous grain boundary layer. The microstructure can be further optimized through heat treatment. In this work, the effect of PrCu on the coercivity of Mischmetal substituted Nd-Fe-B sintered magnets, influence of sintering temperature on microstructure and magnetic properties are studied and the maximum amount of Mischmetal that can be utilized to achieve optimum energy production was identified.

CHAPTER 1. INTRODUCTION

Nd-Fe-B based permanent magnets were discovered independently in the early 1980s at GMRL (General Motors Research Laboratories) [1] and SSMC (Sumitomo Special Metals Corporation) [2]. The fabrication routes used to produce this class of permanent magnets were different for the two companies. Croat et al., used rapid solidification technique to produce R-Fe-B intermetallic compound while Sagawa et al., used a traditional powder metallurgy route that was used to produce Sm-Co permanent magnets. Nd-Fe-B magnets were formally introduced in 1983 at the Conference on Magnetism and Magnetic Materials (MMM) in Pittsburgh, USA [3]. It was reported that properties of these magnets were based on ternary metastable intermetallic compound, $Nd_2Fe_{14}B$ [4]. $Nd_2Fe_{14}B$ alloys achieved the best performance compared to any previously developed hard magnetic materials in terms of intrinsic coercivity (Hcj), remanent magnetization (Br) and maximum energy product (BH)max. Three common routes for the fabrication of bulk NdFeB magnets are – sintering, polymer bonding, and hot deformation. Magnetic properties of these materials had been improved continuously. Currently, the maximum energy product of commercially available sintered NdFeB magnets exceeds 50 MGOe [5]. Over the years, permanent magnets are finding numerous applications on the account of their versatility and economy, ranging from various types of electric motors (servomotors, synchronous motors, spindle and stepper motors, electrical power steering, etc.) to hard disk drive voice coil motors (VCMs), acoustic equipment (microphones, loudspeakers for electronic gadgets like smartphones and laptops, headphones) and magnetic resonance imaging (MRI) instruments [5]. They are crucial components in traction motors for hybrid electric and battery electric vehicles. Furthermore, renewable energy sources like direct drive wind power generators rely heavily on the use of $Nd_2Fe_{14}B$ permanent magnets. Precision applications like permanent

magnet synchronous motors need an understanding of temperature influence on the performance of permanent magnets. Studies found that the magnetic characteristics of sintered $Nd_2Fe_{14}B$ permanent magnets are sensitive to temperature: both the remanence and intrinsic coercivity decrease with the rising of temperature [6]. Motor applications require high stability of coercivity in demagnetizing fields at elevated temperatures. This can be achieved by alloy composition modification with additives like Dy which increases magnetic anisotropy, ensuring superior coercivity values at high temperatures [7], [8].

According to United States Department of Energy's 2011 'The Critical Materials Strategy', five rare-earth elements were found to be critical in the medium term (2015-2025). Out of these five elements two are Dysprosium and Neodymium that are at the top right corner of the importance to clean energy and supply risk plot as shown in Figure 1.1.

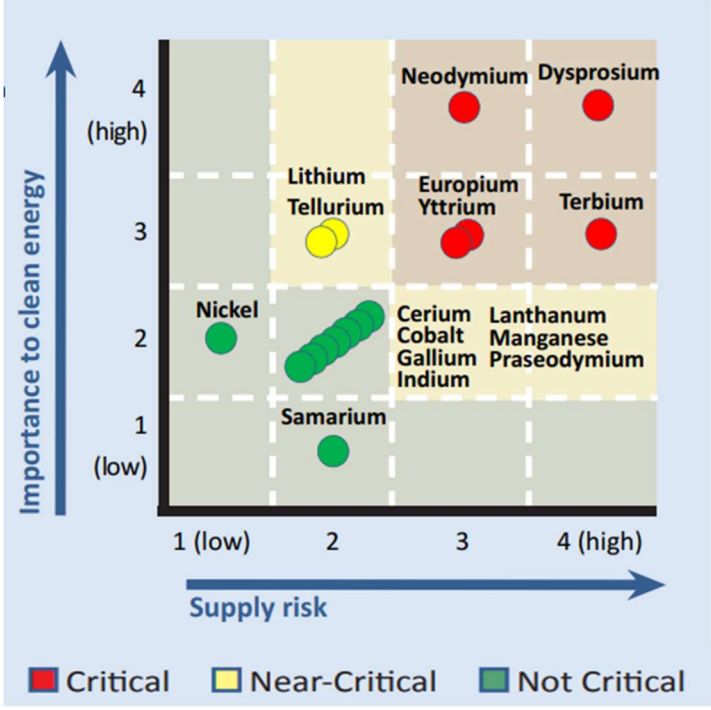

Figure 1.1 Medium-Term (2015-2025) Criticality Matrix [9]

In this context, Nd, indispensable for $Nd_2Fe_{14}B$ permanent magnets, and Dy, a necessary additive for high temperature applications, substantially increased the magnet alloy costs. As the world is advancing towards a sustainable future, the use of wind energy and electric vehicles continues to increase. Since such technologies rely heavily on Nd and Dy, in rare-earth magnets, the demand for two elements is predicted to increase largely and disproportionately. As of 2019, DoE's projected demand for critical minerals show a more than doubling in demand for Nd and Dy from 2010 to 2025 [10].

The balance between the demands of the market and the natural abundances of the REEs in ores is a major concern for the producers of these elements. This is the Balancing Problem [11]. Neodymium has relatively low natural abundance in light rare-earth element ores. Abundant elements like cerium and lanthanum are being stockpiled as they are produced in excess as byproduct of neodymium [12]. One solution to mitigate this problem is finding substitutions for critical elements like neodymium and dysprosium. A good example is Mischmetal (MM), which is an alloy of light REEs, with the REEs in the same atomic ratios as they occur in the REE ores.

Lanthanum, cerium, and MM which have similar electronic structure as Neodymium are much cheaper potential substitutes for Neodymium, albeit the 2-14-1 structure with La,Ce or MM is expected to exhibit smaller magnetic anisotropy field. This work involves the study of MM substitution for Nd in $Nd_2Fe_{14}B$ based sintered permanent magnets. Addition of low melting point alloys like PrCu is proven to be beneficial for coercivity in Dy free NdFeB magnets [13]. The effect of PrCu and sintering conditions on microstructure and magnetic properties of MM substituted sintered magnets is also investigated, aiming for cost reduction and balanced use of raw material resources in $Nd_2Fe_{14}B$-based permanent magnets fabrication.

CHAPTER 2. BACKGROUND

Fundamentals of Magnetism

Everything is made up of atoms, and each atom has a nucleus made of neutrons and protons with electrons that orbit around the nucleus. Magnetism of materials is derived from the motion of electrons within the atoms.

Magnetic fields are produced by moving electric charges. Since the orbiting electrons are tiny moving charges, a small magnetic field is created around each atom. Basically, all the atoms in an object act like several tiny magnets. These magnetic fields have a specific orientation, called the atom's magnetic moment. The magnetic moment of electrons has two distinct sources - orbital motion around the nucleus and spin on its axis. It is expressed by a physical constant called the Bohr magneton (μB).

In most atoms the electrons pair up and spin in opposite directions cancelling their spin magnetic moments and there is a net magnetization of zero. However, in some materials, commonly known as magnetic materials, all or most of these moments align in the same direction creating a magnetic field around itself.

Types of Magnetism

When an external magnetic field is applied to materials, it can induce the alignment of atomic magnetic dipoles within the material. The response of materials to the external field known as degree of magnetization (M), depends on susceptibility (χ) and external magnetic field strength (H).

Magnetic susceptibility is a dimensionless constant that quantifies the extent of magnetization that a material undergoes when subjected to a magnetic field. It can be expressed as ratio of magnetization of a material to the applied magnetic field:

$$\chi = \frac{M}{H}$$

Materials are commonly classified as diamagnetic, paramagnetic, ferromagnetic, ferrimagnetic, and anti-ferromagnetic based on their behavior in a magnetic field.

Diamagnetism

Diamagnetic materials have paired electrons and no permanent magnetic moment. When a magnetic field is applied, the atomic magnetic moments in these materials align in the opposite direction to the field, creating a weak magnetic field that opposes the applied field. Diamagnetic materials exhibit a weak repulsion to an applied magnetic field. However, this effect is relatively weak, and these materials quickly lose their magnetization when the external field is removed.

Diamagnetic materials have a negative magnetic susceptibility very small in magnitude compared to paramagnetic materials and negligible compared to ferromagnetic materials.

Paramagnetism

Paramagnetic materials have unpaired electrons, which possess intrinsic magnetic moments. When subjected to a field, the magnetic moments align in the direction of the field, causing the material to become weakly magnetized. Although the alignment is not as strong as in ferromagnetic materials, they still exhibit a weak magnetism when exposed to a magnetic field. However, these materials lose their magnetism once the external field is removed.

Paramagnetic materials have a positive magnetic susceptibility and unlike diamagnetic materials, it depends on temperature according to the curie law -

$$\chi = \frac{C}{T} \quad [14]$$

C is Curie constant and T is absolute temperature.

Paramagnetic materials are attracted toward magnetic fields while diamagnetic materials are repelled from the field because in diamagnetic materials the internal induced field opposes the external field whereas the paramagnetic state supports it.

Ferromagnetism

Ferromagnetic materials have a spontaneous alignment of atomic magnetic moments, known as magnetic domains. When an external magnetic field is applied, these domains can align in the same direction as the field, resulting in a strong magnetization. The degree of magnetization depends on the strength of the external field. Once the field is removed, these materials can retain some level of magnetization, creating permanent magnets.

Ferromagnetic materials have a very high positive magnetic susceptibility. They exhibit spontaneous magnetization even in the absence of an external field and can be strongly magnetized when a field is applied. However, the relationship between magnetization and applied field is nonlinear in ferromagnetic materials, making their magnetic response more complex.

Above its Curie temperature (T_c) a ferromagnet becomes paramagnetic, and its susceptibility then follows the Curie –Weiss law, with a value of θ (Weiss constant) approximately equal to Tc.

$$\chi = \frac{C}{T-\theta} \text{ [14]}$$

Magneto-crystalline anisotropy

Magneto-crystalline anisotropy is an intrinsic property of a material, and it arises from spin-orbit coupling. Different interactions present in a crystal are –

- **Spin-Spin** - These interactions are very strong but isotropic as they do not depend on the direction of spin axis relative to the crystal lattice and hence cannot contribute to the crystal anisotropy.
- **Spin-Orbit** - When an external field is applied to ferromagnetic materials, it tries to rotate the spin of the electrons. Spin-orbit coupling resists the spin axis rotation and the energy required to overcome it is called anisotropy energy. Spin-Orbit interaction is relatively weak and a smaller field, few hundreds of Oersted, is usually strong enough to overcome this. The applied field also tends to reorient the orbit of electron. However, orbit resists these attempts owing to strong orbit-lattice coupling.
- **Orbit-lattice** - Orbital orientations are fixed very strongly to the lattice and even large fields cannot change them. Due to the strong orbit-lattice coupling, orbital magnetic moments are almost quenched in these crystals.
- **Spin-lattice** – Spin-lattice interactions are very weak and do not affect the anisotropy of a crystal.

Magneto-crystalline anisotropy energy determines the energy required to rotate the magnetization of a material away from its preferred orientation. The energy required to magnetize a crystal is different for each crystallographic direction and the direction in which minimum energy is needed is called easy direction. A crystal with a single easy axis, along which the magnetization can point either up or down, is referred to as a uniaxial crystal. Under these circumstances the anisotropy energy E depends on only a single angle, the angle θ between the Ms (spontaneous magnetization) vector and the c axis (easy axis), and the anisotropy can be described as uniaxial. Many rare-earth transitional metal intermetallic compounds behave this way (uniaxial). The magneto-crystalline anisotropy density can be described as:

$$E = K_0 + K_1 Sin^2\,\theta + K_2 Sin^4\,\theta + \cdots \quad [14]$$

The strength of anisotropy in any crystal is measured by the magnitude of anisotropic constants K_0, K_1, K_2 etc (anisotropic constants are generally measured by torque curves). The magnitude of crystal anisotropy decreases with increasing temperature and becomes zero at curie point. Anisotropy contributes largely to the coercive field and therefore coercive field also becomes zero near curie temperature. Magnetic anisotropy strongly affects the shape of the hysteresis loop.

Magnetic Hysteresis

Ferromagnetic materials are characterized by a nonlinear and irreversible response of magnetization to applied magnetic field. This response is known as hysteresis and is illustrated by hysteresis loop (Figure 2.1)

Hard magnetic materials have broad, square loops indicating once a material is magnetized to saturation it remains in a magnetized state when the field is removed. Therefore, hard magnets are suitable for permanent magnet applications. On the other hand, soft magnetic materials have very narrow hysteresis loops and are considered as temporary magnets as they readily lose their magnetization when the field is removed.

Two important characteristic properties of permanent magnets, coercivity and remanence, are derived from the hysteresis curve. They depend on both intrinsic properties of the material and external features of the material like microstructure, shape etc.

Remanent magnetization Mr (or remanent flux density $Br = \mu_0 Mr$) is defined as the magnetization retained when the applied field is reduced to zero after the sample is saturated. It is directly proportional to spontaneous magnetization and is also affected by degree of alignment, volume fraction of main phase, and density of the material [16].

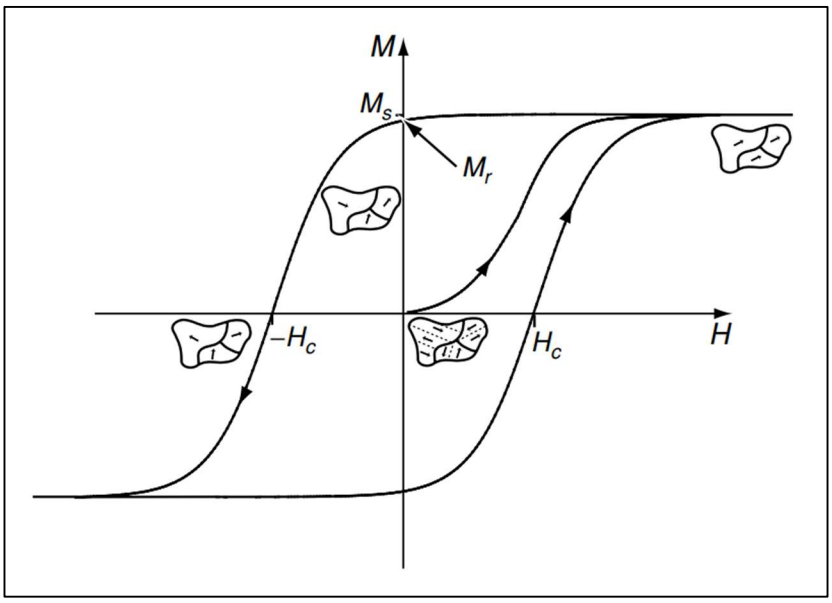

Figure 2.1 Ferromagnetic Hysteresis Loop [15]

Coercivity is the ability of a ferromagnetic material to resist external magnetic field applied in the direction opposite to the alignment of magnetic moment. In other words, it the field required to reduce the magnetization of a material to zero. The coercive field of an ideal magnetic material should be equal to anisotropic field (Stoner–Wohlfarth model). Presently, Hc in the highest grade, commercially available Nd–Fe–B sintered magnets is limited to only ~20–30% of Ha of the $Nd_2Fe_{14}B$ phase (Brown's paradox). One of the reasons for the deviation of coercivity from ideal value is defects in the microstructure which gives coercivity a strong extrinsic nature. Microstructure dependent coercivity can be improved by –

- Reducing grain size [17], [18] – Demagnetization factor increases with grain size [19]. Enhancement of exchange coupling with finer grain size [20].
- Reducing lattice mismatch between main phase and grain boundary layers

- Magnetic isolation of matrix phase – Magnetization reversal propagation is restricted if the grains are magnetically isolated. Formation of continuous and non-magnetic grain boundaries enhances decoupling [21].
- Rounded main phase grains – Sharp edges act as nucleation sites for reverse magnetic domains [22].

The hysteresis loop also carries information on spontaneous magnetization. It is an intrinsic magnetic property which exists within a ferromagnetic domain. When external magnetic field is applied on a material, spontaneous magnetization changes direction and reaches saturated state. It arises from the alignment of magnetic moments and reaches saturated state. Above curie temperature, spontaneous magnetization becomes zero as the material loses magnetic ordering [15].

Maximum energy product (BH)max is energy density that is often used to denote the grade of commercial magnets. It is defined as the maximum value of product the of B and H along the demagnetization curve (second quadrant of the hysteresis loop). Here, B=M+H.

$Nd_2Fe_{14}B$ Based Alloys

The $Nd_2Fe_{14}B$ crystal lattice has tetragonal symmetry (space group P42/mnm), and each unit cell contains 4 formula units or 68 atoms. Within the unit cell, there are six crystallographically distinct Fe sites, two different rare-earth positions, and one B site [23].

Magnetic behavior of 2:14:1 compounds primarily arises from the interplay between rare-earth crystalline electric field and rare-earth-iron exchange interactions. For $Nd_2Fe_{14}B$, rare-earth contributes to magneto-crystalline anisotropy whereas iron sublattice provides most of the magnetization [23].

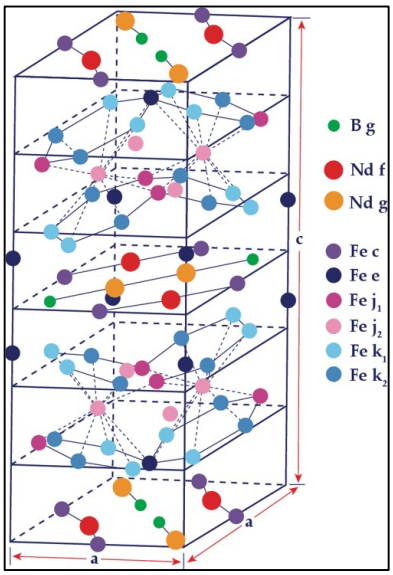

Figure 2.2 Tetragonal $Nd_2Fe_{14}B$ Unit cell (c/a ratio is not to scale) [4].

All $RE_2Fe_{14}B$ compounds have structure isomorphous to $Nd_2Fe_{14}B$. Lattice constants of $RE_2Fe_{14}B$ tetragonal compounds decrease with increasing atomic number which is related to trivalent lanthanide contraction effect [24]. Room temperature lattice constants along with intrinsic magnetic properties for some $RE_2Fe_{14}B$ compounds are listed in table.

Table 2.1 Room Temperature Lattice Constants (a&c), Saturation Magnetization (Ms), Anisotropy Field (Ha), and Curie Temperature (Tc) of Selected $RE_2Fe_{14}B$ Compounds [23].

Compound	**a(Å)**	**c (Å)**	**4πMs (KG)**	**Ha (KOe)**	**Tc (°C)**
$La_2Fe_{14}B$	8.82	12.32	13.8	20	257
$Ce_2Fe_{14}B$	8.76	12.11	11.7	26	151
$Pr_2Fe_{14}B$	8.8	12.23	15.6	75	292
$Nd_2Fe_{14}B$	8.8	12.2	16	73	312
$Tb_2Fe_{14}B$	8.77	12.05	7	220	347
$Dy_2Fe_{14}B$	8.76	12.01	7.1	150	325

Substitution of Nd in $Nd_2Fe_{14}B$ by Dy and Tb significantly enhances anisotropy but reduces saturation magnetization because in heavy rare-earth elements, R-Fe moment coupling is antiparallel that implies rare-earth and iron moments are coupled antiferromagnetically whereas R-Fe moments are coupled ferromagnetically for light rare-earth elements.

In contradiction to trivalent lanthanide contraction trend, lattice constants of $Ce_2Fe_{14}B$ compound are smaller than that of $Pr_2Fe_{14}B$ and $Nd_2Fe_{14}B$. This indicates the tetravalent or mixed valence state of Ce (Ce^{+3}, $Ce^{+4)}$ in $Ce_2Fe_{14}B$. Neither Ce^{4+} nor La^{+3} carries magnetic moment. For compounds with zero orbital moment, both magneto-crystalline anisotropy and magnetization are provided by iron sublattice alone [25].

Three types of interactions are possible among R and Fe moments – R-R, R-Fe, and Fe-Fe. The Curie temperature of $R_2Fe_{14}B$ systems depends on these interactions. The Fe-Fe exchange is direct and is the strongest interaction and depends on Fe-Fe separation. Due to shorter Fe-Fe distances in $R_2Fe_{14}B$ compounds, the exchange between them is antiferromagnetic (negative interactions) [26], [27]. Therefore, the curie temperature of $R_2Fe_{14}B$ compounds is significantly lower than that of pure Iron, 770 °C. Co-Co and Co-Fe exchange interactions are positive (ferromagnetic) and therefore partially replacing Fe by Co increases curie temperature but deteriorate magnetic properties. Tc of $Nd_2Fe_{14-x}Co_xB$ increases from 312 °C at x = 0 to 427 °C at x = 2, reaching 727 °C for $Nd_2Co_{14}B$. However, this increase in Tc comes at the expense of Ms and Ha. A maximum of Ms (~ 34 μB/f.u.) is obtained at x = 2 [23].

Phase Diagram of NdFeB

Phase diagrams provide information on behavior of materials such as crystal structures, solubility, thermal expansions, phase transformation etc. Therefore, they are extensively used in materials designing and processing.

The phase diagram of Nd-Fe-B system consists of three ternary compounds: $Nd_2Fe_{14}B$, $Nd_2Fe_7B_6$, and $Nd_{15}Fe_{77}B_8$. $Nd_2Fe_{14}B$ which is the matrix phase in Nd-Fe-B permanent magnets is formed by a peritectic reaction between Fe and the liquid [28]. In addition to $Nd_2Fe_{14}B$, sintered Nd-Fe-B magnets consists of Nd-rich phases, $Nd_{1+\varepsilon}Fe_4B_4$, and Nd oxides [23]. $Nd_2Fe_{14}B$ is a hard magnetic phase and remanence depends on the volume fraction of this phase present in the alloy. Formation of Nd-rich intergranular phases is essential to fabricate high coercivity sintered magnets as these phases are non-magnetic thereby providing magnetic isolation to adjacent $Nd_2Fe_{14}B$ grains [29].

Nd-Fe-B Sintered Magnets Fabrication Techniques

Strip casting

Strip casting is a rapid solidification technique that is used to produce thicker ribbons or flakes. It involves induction melting of an alloy and ejecting the liquid onto a rotating water-cooled Copper wheel through a crucible orifice. Cooling rates as high as 10^3-10^4 K/s, depending on the surface velocity of the wheel can be achieved by this method. The fast-cooling rate in strip casting avoid the formation of free alpha-Fe phase, which enhances the magnetic properties of the resulting NdFeB magnets. The microstructure of the strip-cast material features $Nd_2Fe_{14}B$ grains with plate-like shapes surrounded by a thinly distributed Nd-rich phase and it significantly affects the particle size of powders that were obtained by subsequent milling processes which in turn affects the magnetic properties of the sintered magnet.

Conventional ingot casting for sintered magnets forms high amounts of alpha-Fe dendrites and Nd-rich regions which is detrimental to magnetic properties. The rapid cooling rates offered in strip casting suppress the formation of alpha-Fe and Nd-rich phases and produce homogeneous and fine scaled microstructures [30]. However, there is an optimal cooling rate to

obtain an ideal microstructure. Higher cooling rates will produce smaller grains, which make it difficult to be milled into single crystal particles and consequently creating difficulty during the field-alignment process before sintering, whereas lower cooling rates deteriorate magnetic properties due to the precipitation of soft iron phase [31]. In addition, the fine and uniform size of the columnar structure in the strip cast alloys is beneficial for the milling process to prepare powders with uniform particle size [32].

The microstructure obtained by strip casting has three main advantages over conventional casting methods: the distribution of Nd-rich phases is fine and thus less sensitive to oxidation, the absence of α-Fe and the fine obtained grain size after milling; all lead to coercivity improvement.

Hydrogen Decrepitation

Hydrogen decrepitation involves exposing strip cast alloy to hydrogen to help break the alloy into small particles. The process can be carried out at high pressure or high temperature to help speed up the process. Hydrogen is a very small and reactive atom that easily penetrates the grain boundaries of many metals. Hydrogen embrittles metals by entering the grain boundaries and creating pressure at the weakest point. This causes micro-cracks that begin to propagate through the grain structure.

Because of the inter-granular nature of the decrepitation process the final particle size will depend on the initial grain size of the alloy and on the distribution of the neodymium-rich phase [33]. Hydrogen is readily absorbed by Nd rich grain boundaries and decrepitation takes place because of the formation of NdH_{2+x} and consequent differential expansion which leads to grain boundary failure [34].

In 1979, Harris et al. [35] reported the hydrogen treatment of $SmCo_5$ and Sm_2Co_{17} alloys and it was later applied to the $Nd_2Fe_{14}B$ system. For $Nd_2Fe_{14}B$ alloys, the process involves the

room temperature exposure of the cast material to hydrogen gas in an evacuated jar at high pressure. Hydrogen is absorbed along the grain boundaries diffused into the Nd-rich intergranular phase to form NdH_{2+x}. Hydrogen absorption is dissociative in these materials; molecular hydrogen being dissociated into hydrogen. The presence of the Nd-rich phase plays a crucial role in absorbing hydrogen readily at room temperature while the $Nd_2Fe_{14}B$ phase material absorbs hydrogen at around 160 °C [36]. Decrepitation occurs due to the differential volume expansion upon hydrogenation between the $Nd_2Fe_{14}B$ phase and the Nd-rich phase (volume increase of 4.8 % and 16.4 % respectively) and the material is thus turned into friable powder. The brittle coarse powder resulted after HD is milled and further used for the fabrication of sintered magnets which is performed in vacuum to facilitate hydrogen thermal desorption.

Dehydrogenation is facilitated during the sintering of magnets where thermal desorption of Hydrogen takes place in three stages, from the main phase at 200 °C and then from the Nd-rich phase, in two steps - NdH_3 to NdH_2 at 250 °C and NdH_2 to Nd at 600 °C [37]. The hydrogen absorption-desorption behavior is influenced by the composition and the microstructure of the cast alloy.

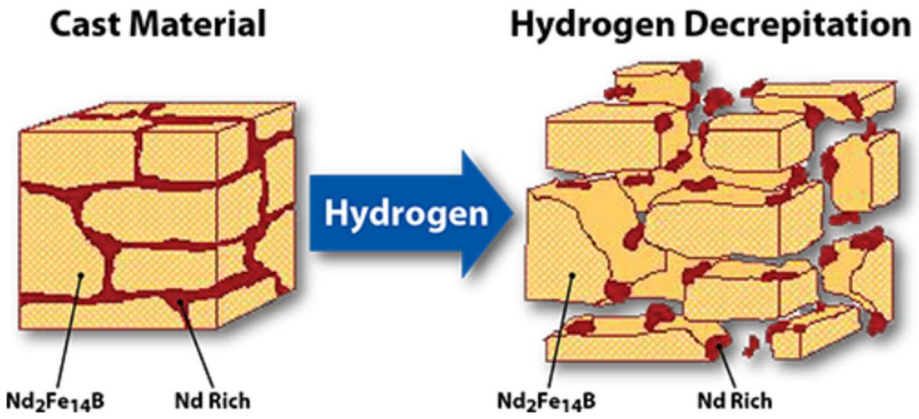

Figure 2.3 Hydrogen Decrepitation in $Nd_2Fe_{14}B$ Systems [38].

Ball Milling

To achieve high-energy product in Nd-Fe-B sintered magnets, it is important to have small particles and narrow particle size distribution, high degree of alignment of the C-axis, and high control of oxygen contamination. The latter is significant as oxygen affects the hard magnetic properties of the sintered magnets. Most of the oxygen contamination occurs during the milling stage. Maintaining oxygen content < 2000ppm is essential to obtain high (BH)max magnets.

Magnetic Alignment

It is easy to align the powder when the particles are still loose and not agglomerated. If the individual particles are single crystals, application of strong magnetic field aligns the easy axis of powder particles parallel to the applied field. This alignment will be locked after pressing the powder. Alignment will not occur if each particle is polycrystal [14].

Cold Isostatic Pressing (CIP)

It is crucial to compact the powder without disturbing the alignment of particles achieved in the previous step. Isostatic pressing applies equal pressure in all directions on a powder compact thus achieving maximum uniformity of density and microstructure without the geometrical limitations of uniaxial pressing.

Sintering

The green compact formed by CIP is further densified by sintering. The main objectives of sintering are - liquidus phase formation to fill pores and solid-state diffusion. Sintering is carried out below the melting temperature of the main phase and above the melting temperature of Nd-rich phase and other grain boundary phases. The sintering temperature should be high enough for the formation of liquidus grain boundary phases but should not lead to excessive

grain growth. Holding at sintering temperature for longer time may also lead to grain coarsening. However, holding time should be long enough for the liquidus phase to fill voids and surround the main phase grains.

Heat treatment

Annealing heat treatment is performed post sintering to enhance coercivity which depends on various microstructural features. Optimal annealing cycle ensures the uniform distribution of Nd-rich phase, smoothening of grain boundaries and reduction of defect density. The addition of elements like Cu increases the wettability of the main phase during sintering and post sintering treatments which is discussed in later sections. After annealing, the quantity of hard magnetic phase might increase by the reaction of excess Fe with Nd-rich phases.

Cerium/Lanthanum Substituted $Nd_2Fe_{14}B$ Permanent Magnets.

Substituting Nd with Ce and La will result in poor magnetic performance due to poor intrinsic properties of $Ce_2Fe_{14}B$ and $La_2Fe_{14}B$ (Table 2.1). However, Ce and La substituted permanent magnets gained a lot of attention owing to their high abundance and low cost. Solidification and microstructural behavior of few Ce and La substituted Nd-Fe-B permanent magnets are reported in this section.

At Ce fractions below 30 wt.% of the rare-earth content, Ce partly substitutes Nd in the intergranular material forming the (Ce, Nd)-rich phase which has lower melting point than the typical Nd-rich phases [39]. At higher Ce concentrations, $CeFe_2$ segregation occurs in substituted magnets. The melting point of $CeFe_2$ phase is 925 °C which means this phase melts during sintering and hence increases the volume fraction of liquidous phase which is conducive to the formation of continuous grain boundary layers. However, $CeFe_2$ being paramagnetic at room temperature decreases remanence magnetization [40].

It is also reported that with increase in Ce content, the grain boundary layer becomes thicker and more continuous which can be attributed to the formation of $CeFe_2$ phase [41]. $CeFe_2$ phase will form when Ce substitution for Nd-Pr is greater than 25 wt% in $(NdPr)_2Fe_{14}B$ magnets. Due to the formation of $CeFe_2$, volume fraction of the main 2-14-1phase decreases, which rapidly reduces Ms for magnets at high Ce substitution [41].

It is shown that addition of La to Ce substituted Nd-Fe-B alloys suppress the formation of paramagnetic $CeFe_2$ phase and thus the volume fraction of main phase increases [42]. Also, resistance to oxidation improves with La addition [43]. This enhances remanence and maximum energy product. However, coercivity drops with increase in La substitution due to the lower anisotropic field of $La_2Fe_{14}B$ (20 KOe) as compared to $Ce_2Fe_{14}B$ (26 KOe) and discontinuous grain boundary layers because of reduced $CeFe_2$ content in La substituted magnets.

The curie temperature of $(Ce_{1-x}La_x)_2Fe_{14}B$ melt-spun alloys is found to increase from 420K to 476 K when x is increased from 0 to 0.5 which is due to the fact that the Tc of $La_2Fe_{14}B$ and $Ce_2Fe_{14}B$ is 257 °C and 151 °C, respectively [44]. $CeFe_2$ phase can be totally suppressed with more than 20 atom% La substitution for Ce and at 30 atom% La substitution, significant grain refinement is identified in (La,Ce)-Fe-B melt spun ribbons.

Unlike $Nd_2Fe_{14}B$ and $Ce_2Fe_{14}B$ phases, $La_2Fe_{14}B$ is hard to obtain from La-Fe-B alloy as this phase is unstable. Melt-spun $La_2Fe_{14}B$ alloy mostly consists of α-Fe and La phase [45], [46]. Substitution of at least 10% Nd for La favors the formation of 2:14:1 phase in La-Fe-B alloys [45].

Mischmetal Substituted $Nd_2Fe_{14}B$ Permanent Magnets

Mischmetal (MM) is mined as raw ore with a composition of La and Ce accounts about 80%, and rest is Pr and Nd. MM doesn't need the separation of these elements and therefore

using MM to substitute Nd could reduce the purification cost. However, a common definition of modern MM is $LaCe_3$ due to high demand for Pr and Nd and the development of advanced processing methods. Moreover, increasing the use of MM-Fe-B magnets leads to balanced utilization of rare-earth elements and the environment pollution will be reduced and hence MM has gained a lot of importance in recent years.

The coercivity significantly deteriorates at higher MM substitution for Nd in Nd-Fe-B magnets due to the low magneto-crystalline anisotropy of (La,Ce)-Fe-B (Table 2.1). Coercivity can be improved by refining the grains. However smaller powders are prone to oxidation as Ce and La oxidize easily.

Chen et.al [32] reported coercivity of 9.61 KOe in $Nd_{0.5}MM_{0.5}$-Fe-B (MM contains 27.49 wt% La, 53.93 wt% Ce, 1.86 wt% Pr and 16.72 wt% Nd) sintered magnet. Such high coercivity is obtained by fine particle size and optimizing annealing temperature that gives continuous grain boundaries. Antioxidants are added to control oxygen contamination during jet milling.

Liu et.al [47] reported coercivity enhancement of sintered $MM_2Fe_{14}B$ (MM contains 25 wt% La, 55 wt% Ce, 5 wt% Pr and 15 wt% Nd) magnets by grain boundary diffusion of TbH_x nanoparticles. Tb is observed to enrich the surface of $MM_2Fe_{14}B$ phase forming $(MM\text{-}Tb)_2Fe_{14}B$ which has higher Ha than $MM_2Fe_{14}B$.

Shang et.al [48] reported that the lattice constants of $MM_2Fe_{14}B$ are smaller than that of $Nd_2Fe_{14}B$ which is due to the mixed valence of Cerium, Ce^{+3} and Ce^{+4} (The radius of Ce^{+4} is smaller than that of Nd^{+3}). For $MM_{14}Fe_{79.9}B_{6.1}$ magnets, no significant change is observed in Hcj and (BH)max with increase in sintering temperature from 1000 °C to 1040 °C. However, these properties are reduced drastically when the samples are sintered at above 1040 °C. The atom %

of Ce and Pr in the main phase grains is about the same as in MM composition whereas La is reduced by 7.5 atom % and Nd is increased by the same amount in the matrix phase. The reduction in La content is attributed to the unstable nature $La_2Fe_{14}B$ phase.

Xiong et.al [49] prepared MM substituted $Nd_2Fe_{14}B$ sintered magnets by dual alloy method. In these magnets, three matrix phases instead of two were observed which indicates that that the two initial magnetic phases, $Nd_2Fe_{14}B$ and $MM_2Fe_{14}B$ diffused into each other during sintering. This can lead to a reduction in coercivity due to the formation of local regions with low anisotropic field. Li et.al [50] reported a method that prevents the diffusion of Nd-rich and La/Ce rich main phases into each other during sintering which therefore enhances coercivity. This is achieved by regulating elemental distribution of sintered MM-Fe-B magnets prepared by dual main phase alloy method where Nd-Fe-B powders with little higher Nd content and (MM,Nd)-Fe-B powders with reduced MM-Nd content were used. In 40wt% MM content in RE sample, the properties of the magnet prepared by this method are better than magnets with same MM content.

PrCu Addition to Nd2Fe14B Permanent Magnets

One approach to develop Dy-free high coercivity NdFeB magnets is magnetically isolating matrix grains by formation of continuous intergranular phases. The addition of low melting point elements like Al, Cu, and Ga are proven to be beneficial for coercivity enhancement. In this work, 7.5 wt% $Pr_{68}Cu_{32}$ alloy is added to $(NdMM)_2Fe_{14}B$ for coercivity improvement. PrCu alloy has eutectic transformation at around 480 °C. Cu decreases the melting point of Nd-rich phases and therefore improves wettability (which leads to the formation of rounder main phase grains) and continuity of grain boundary phases during sintering and post sintering treatments.

It is reported [51] that low temperature annealing, at ~480 °C is effective for coercivity enhancement in samples with PrCu addition whereas annealing at same temperature shows negative effect on coercivity in samples without any addition. The increase of coercivity is attributed to segregation of Cu from Cu rich phase to Cu-lower phase. Annealing above and below optimum temperature decreases coercivity by a significant amount. The volume fraction of grain boundary phases increases with an increase in PrCu content. Continuous and distinct grain boundaries are observed in the samples where PrCu is added and annealed at 480 °C and also grain size increases and becomes less uniform in increase in the amount of PrCu. It is reported that more than 0.15 at.% Cu addition drastically reduces magnetic properties due to grain coarsening and formation of pores [52]. It is also observed that Pr substitutes Nd in the main phase during sintering.

Wan et.al, [53] reported that grain size decreases, and grain boundary layer becomes thicker, smoother, and more continuous with PrCu addition. The volume fraction of ferromagnetic phases at grain boundaries decreases with the addition of PrCu.

Coercivity enhancement through PrCu is mainly due to the following reasons –

- PrCu smoothens the grain boundaries –Hindering the nucleation of reverse magnetic domains.
- PrCu increases the thickness of grain boundaries – Providing magnetic isolation to the grains, that means reverse magnetization won't propagate once the reverse magnetic domains form at defects/sharp edges.
- PrCu reduces the ferromagnetic phases at grain boundaries–Reducing the exchange coupling between the grains and hence slows down reverse domain expansion.

CHAPTER 3. EXPERIMENTAL TECHNIQUES

Magnet Fabrication

Base alloy preparation

Alloy samples of nominal composition $(Nd_{1-x}MM_x)_{2.64}Fe_{12}Co_2B_{1.06}$, x=0 to 1, were prepared by arc melting the samples under argon atmosphere using an arc melter. The samples were flipped and melted multiple times to obtain a uniform composition.

The ingot samples obtained after arc melting were used to produce strip-cast ribbons in melt spinner. During strip casting, the ingot in a quartz tube of 1.1mm nozzle was induction melted in an evacuated chamber backfilled with helium and ejected at 200 Torr onto a copper wheel rotating at 2 m/s. Parameters used for strip casting are shown in Table 3.1.

Table 3.1 Strip-cast Parameters

Wheel speed	2 m/s
Chamber pressure	1/3 Atm
Chamber gas	Helium
Ejection pressure	200 Torr
Ejection temperature	1300 °C
Orifice diameter	1.1 mm

To obtain coarse powder strip cast flakes (Figure 3.1.a) were hydrogen decrepitated at room temperature under 400 KPa H_2 pressure. Hydrogen decrepitation (HD) operation was carried out in a stainless-steel jar connected to vacuum and hydrogen pipe systems. The HD jar was flushed with nitrogen three times before introducing hydrogen at 400Kpa pressure, and the

HD process was carried out for 5 hours at room temperature. The HD jar was evacuated and transferred to the glove box for the decrepitated flakes to be collected for further steps.

The flakes were loaded into a ball milling jar and 7.5wt% PrCu powder was added to the base alloy for some samples according to the designed formula. The jar was filled with cyclohexane and milled in a low energy ball miller (Figure 3.1.b) at 206 rpm for thirteen hours. The ball milled powder was transferred into a glove box under nitrogen atmosphere and was collected and sieved using a 75 μm sieve. The collected powder was put into a cylindrical rubber die of diameter 12 mm and of height 12 mm. In the glove box, the risk of oxidation of the powder is minimum. The die with the powder was then put into a nitrile glove which was sealed under vacuum as further magnetic alignment and pressing steps are performed outside of the glove box.

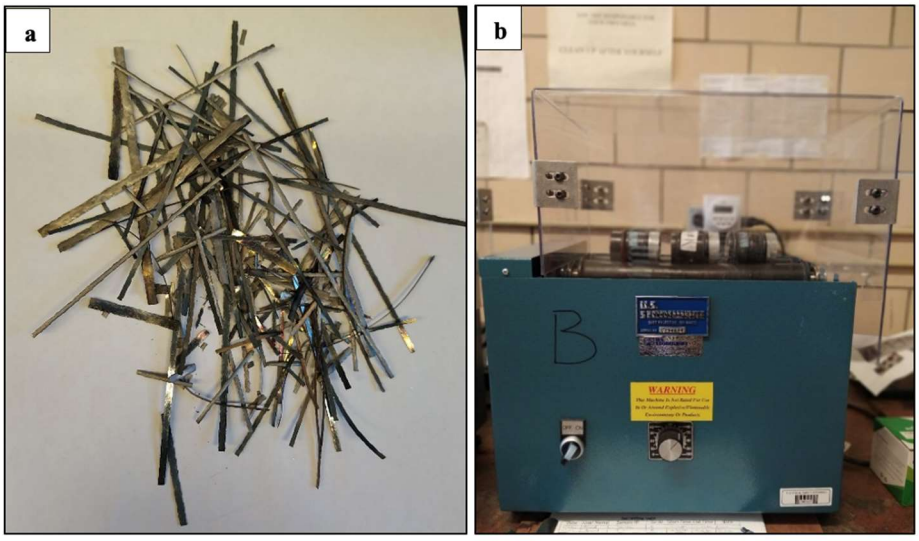

Figure 3.1a. Mischmetal Strip-cast and b. Roller Jar Milling Unit.

Alignment of the powder was performed with a pulsed Magnetizer under 9 Tesla field. To ensure optimum orientation, consecutive magnetic pulses of opposite direction were applied three times. The aligned powder was pressed isostatically at room temperature (CIP – Cold

Isostatic Pressing). For CIP (Figure 3.2.a), the die was placed into a vessel filled with oil and loaded into a press where a load of 500 MPa was applied for 1 minute.

The green compact obtained after CIP was loaded into the sintering holder in a glove box and then loaded into a vertical sintering furnace (Figure 3.2.b). When the vacuum reaches less than $3x10^{-5}$ Torr, the furnace power was turned on at a heating rate of 900 °C/hr. The samples were sintered between 1060 -1080 °C for 1.5-3 hours and were quenched by dropping the sample into a water-cooled cup at the bottom of the furnace. After the furnace was back filled with argon and cooled down to 50 °C or below, the samples were unloaded.

Figure 3.2 Image Showing a. Press Used for CIP and b. Vertical Sintering Furnace.

The sintering process was carried out in various steps. Once the furnace temperature reaches the desired temperature, the sample is lowered in stages to ensure the removal of residual hydrogen from Nd-hydrides that are formed during hydrogen decrepitation process.

Sintered samples were sealed in quartz tube (Figure 3.3.b) for post-annealing that is carried out in a box-furnace Figure 3.3.a). The heat treatment cycle used for these samples is as

follows: 580 °C for 2 hours, 500 °C for 3 hours, 480 °C for 5 hours, 460 °C for 24 hours, and 440 °C for 24 hours. After annealing, the samples were quenched in water.

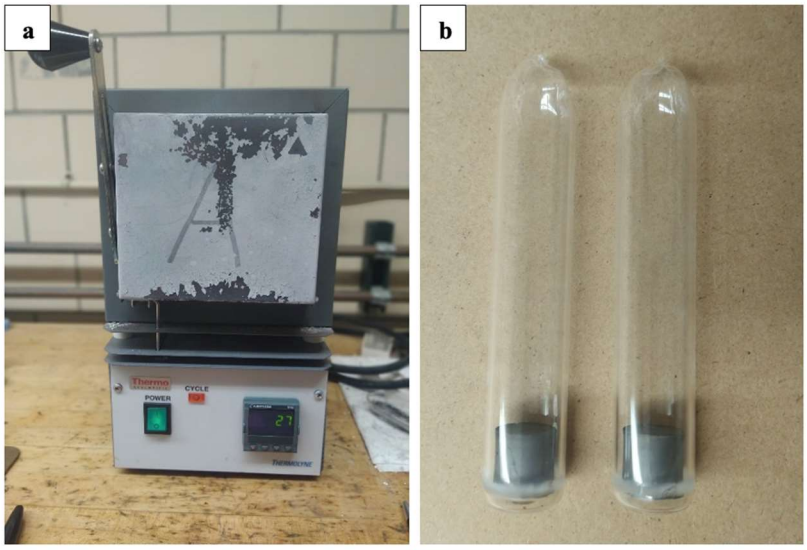

Figure 3.3 Image Showing a. Annealing Furnace and b. Sintered Samples Sealed in Quartz Tube

PrCu alloy preparation

The alloy of composition $Pr_{68}Cu_{32}$ was prepared by arc melting. Ribbons from arc melted ingot were obtained by melting spinning and the parameters used are summarized in Table 3.2.

Table 3.2 Melt Spin Parameters Used for Preparing PrCu Ribbons

Wheel speed	20 m/s
Chamber pressure	1/3 Atm
Chamber gas	Helium
Ejection pressure	150 Torr
Ejection temperature	1000 °C
Orifice diameter	1.1 mm

Melt spun ribbons (Figure 3.4) were ball milled using low roller ball miller for 15 hours at 205 rpm. The fine powder was collected sieved through 75µm mesh. This powder was mixed with base alloy strip cast in 7.5 wt% and milled for 13 hours as described in above section.

Figure 3.4 PrCu Melt-spun Ribbons.

Characterization Techniques

Magnetic Measurements

The hysteresis loop measurements of the mischmetal magnets were carried out at room temperature using Hysteresisgraph AMH-500 BH-Tracer. This instrument uses large samples. No sample cutting is required for these measurements. The samples after heat treatment were used for the more physical property measurement. The density of the samples was measured by Archimedes principle. In this work, the sample size is generally around 10 mm (height) and 10 mm (diameter) after sintering. The input parameters are the sample height, diameter, mass, and density.

During the hysteresis loop measurement, the sample was inserted within the airgap of a magnetic circuit (Figure 3.5 center) situated between two poles made of Fe-Co. The sample

surfaces were polished to obtain a plane surface to avoid undesired air gap between the sample and the poles as air gap or irregularities at the sample surface reduce the measured remanence.

The sample is inserted inside the circular hole of the coil (Figure 3.5 Right). The first and second quadrant of the hysteresis loop are measured. A maximum magnetic field of 18KOe is applied. LJ compensated coils of 15mm, and pole LP-80 mm were used.

The B-H tracer characterizes the demagnetization curve of the measured magnet. Magnetic properties such as saturation (Jmax), remanence (Br), coercivity (Hcj), and maximum energy product ((BH)max) can be determined instantly as well as the squareness or rectangularity which is the ratio of Hknee (the value of the field for which magnetization value is 0.9MR) to Hcj. A magnet with high squareness (close to 1) is preferred for the magnet application.

Figure 3.5 B-H Tracer

Microstructure and Composition Analysis

Scanning Electron Microscopy

Scanning electron microscopic analysis for samples in the work is done by using FEI Teneo LoVac (Field-Emission Scanning Electron Microscopy) and FEI Inspect F50 Scanning Electron Microscope. Small samples of size 3x6 mm were cut from bulk sample using EDM. Sample preparation on SEM involved mounting the sample in epoxy resin, grinding and

mechanical polishing. The polished samples were sputter coated with thin layer of gold on the surface for conduction.

The SEM has a large depth of field, which allows a large amount of the sample to be in focus at one time. The SEM also produces images of high resolution, which means that closely spaced features can be examined at a high magnification. Preparation of the samples is relatively easy since most SEMs only require the sample to be conductive. The combination of higher magnification, larger depth of focus, greater resolution, and ease of sample observation makes the SEM one of the most heavily used instruments in research areas today [54].

When an electron beam strikes a sample a large number of signals are generated as shown in Figure 3.6. The most used signals in SEM are Secondary electrons, back scattered electrons, and X-rays and they carry different types of information.

Back scattered electrons originate from a wide and deeper region within the interaction volume. They occur due to elastic collisions of electrons with atoms. Larger atoms create higher signal as compared to small atoms as the former scatter electrons more strongly. Therefore, the strength of signal from backscattered electrons is proportional to their atomic number (Z); the higher the atomic number, the brighter the material appears in the image. This sensitivity to atomic number helps to distinguish between different phases, providing imaging that carries information on the sample's composition.

In contrast, secondary electrons originate from the surface regions of the sample. They occur due to inelastic interactions between the primary electron beam and the sample and contain lower energy than the backscattered electrons. Secondary electrons provide very beneficial information on topography of the sample's surface. The contrast is obtained from the difference

in height on the surface because the generation of secondary electrons depends on the angle of incidence between the beam and the sample.

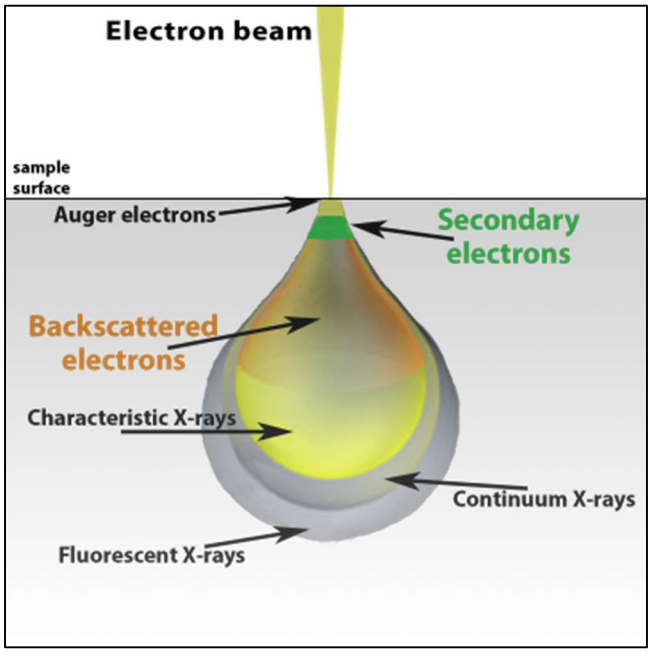

Figure 3.6 Electron-specimen Interaction Volume and Signals Generated [55].

Energy-Dispersive X-Ray Spectroscopy

EDX analysis was performed by Oxford Aztec energy dispersive detector (EDS). Both the SEMs mentioned above are equipped with EDS detectors. EDX can be used for both qualitative and quantitative analysis, it helps to identify both the type of elements that are present as well as the percentage of each element's concentration within the sample.

Characteristic X-rays are generated using EDX following the following process. The electron beam hits the inner shell of an atom, knocking off an electron from the shell, while leaving a positively charged electron hole. When the electron is displaced, it attracts another electron from an outer shell to fill the vacancy (Figure 3.7). As the electron moves from the outer

higher-energy to the inner lower-energy shell of the atom, this energy difference can be released in the form of an X-ray. The energy of this X-ray is unique to the specific element and transition thus allowing its identification.

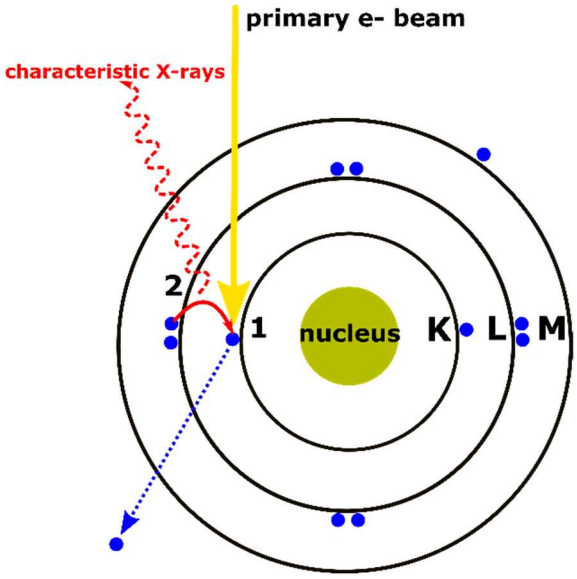

Figure 3.7 Generation of Characteristic X-rays [56].

CHAPTER 4. RESULTS

This chapter is divided into three sections - effect of misch metal content, effect of sintering temperature, and effect of PrCu addition on the microstructure and magnetic properties of MM substituted Nd-Fe-B sintered magnets. Magnetic properties at elevated temperatures are also studied.

Effect of Mischmetal content

This subchapter contains the study on the influence of MM substitution on the phase composition, microstructure, and magnetic properties of the $(Nd_{1-x}MM_x)_{2.64}Fe_{12}Co_2B_{1.06}$ (x=0, 0.2, 0.3, 0.4, 0.5, 0.6, 0.7, and 1) sintered magnets. The magnets will be referred to as MM followed by weight % of MM in the composition (Example – MM30 for x = 0.3 sample). Here, the MM composition is about 30 wt.% La, 60 wt% Ce, and 10 wt% Nd. Unless specified all the magnets were added with 7.5 wt. % PrCu. Samples were sintered at 1060 °C and 1080 °C. S1060 is used to refer samples that were sintered at 1060 °C for 3 hours and S1080 is used to indicate that the sample is sintered at 1080 °C for 1.5 hours. Samples that do not have PrCu additives are specified as no-add meaning no additives were added to the base alloy.

S1080

Microstructural Analysis

Figure 4.1 contains SEM images showing the microstructure of the MM substituted magnets sintered at 1080 °C for 1.5 hours for MM = 30, 40, 60, 70 and 100 weight percent substitution. In these images gray contrast corresponds to the matrix 2-14-1 phase and the bright contrast is related to the intergranular RE-rich phases.

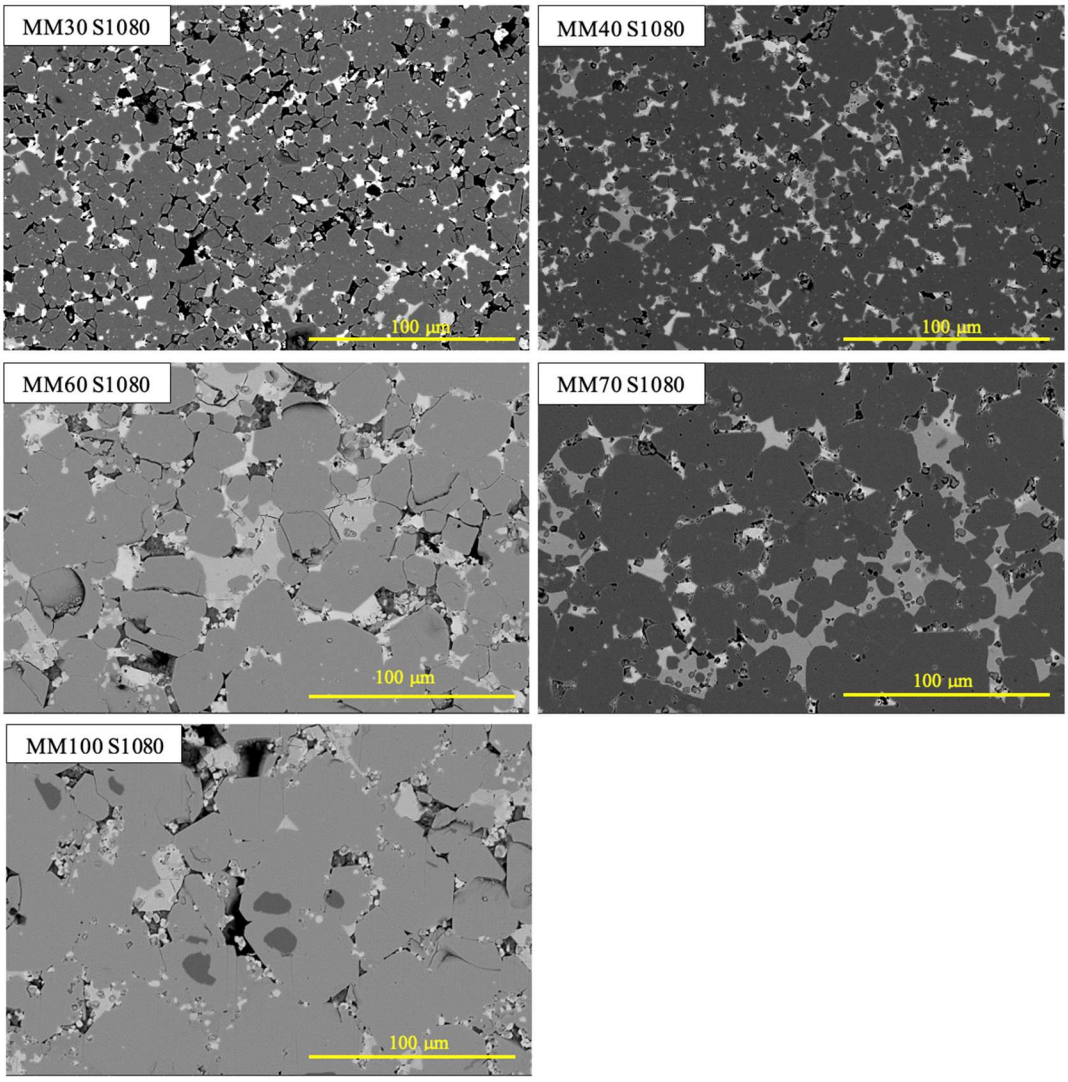

Figure 4.1 BSE Image of MM30, MM40, MM70, and MM100 magnets with 7.5% PrCu addition sintered at 1080 °C for 1.5 hours.

Since all the electron images in figure were taken at same magnification, it can be clearly seen that Ce substitution induced grain growth. The morphology of grain distribution in all the magnets is very similar except for different grain sizes. The grain distribution is not very uniform in all these magnets, and for MM40 average grain size is about 5.7 µm, which increases six-fold to 38 µm for the MM100 sample indicating much coarser grains in MM100 magnet.

In Figure 4.2 the concentration of La, Ce, and Nd elements going through the rare-earth rich grain boundary phase and the $Nd_2Fe_{14}B$ matrix phase grains are shown. The X-axis of these plots are MM content in total rare earth elements that was added to the base alloy, and the Y-axis represents the element weight fraction in the microstructure.

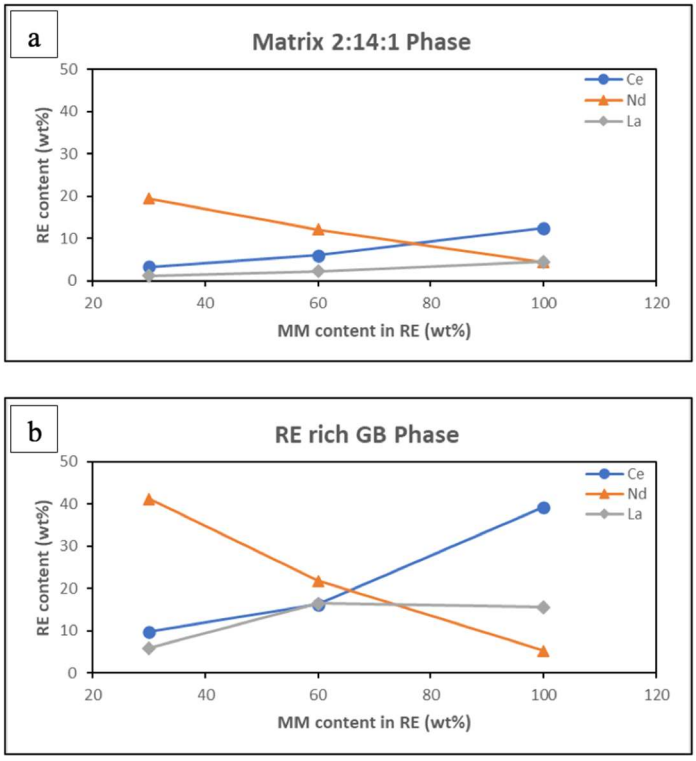

Figure 4.2 Rare-earth element distribution in a. matrix phase and b. grain boundary phase

Figure 4.2a shows the individual rare earth element concentrations in the matrix phase, whereas Figure 4.2b the elemental distribution in rare earth-rich grain boundary phases. From the plots, it is evident that with increase in MM content La and Ce fractions in the matrix 2:14:1 Phase increases whereas Nd content decreases. Similar behavior is observed in the grain boundary region, the amount of Nd decreases whereas Ce content increases with increasing MM

content. However, improvement of Ce content in the rare-earth rich grain boundary phase is bigger than that in the matrix phase which means that Ce is tending to diffuse into the rare-earth rich phase instead of $Nd_2Fe_{14}B$ matrix phase grains.

Similarly, La also tends to be expelled from the matrix phase. Consequently, the grain boundary became thicker and more defined in higher MM content magnets. The thicker grain boundary favors the isolation of adjacent hard magnetic grains, and thus leads to improvement of coercivity. That means microstructure compensates for the reduction in coercivity due to low anisotropic field of Ce and La 2:14:1 compounds to some extent.

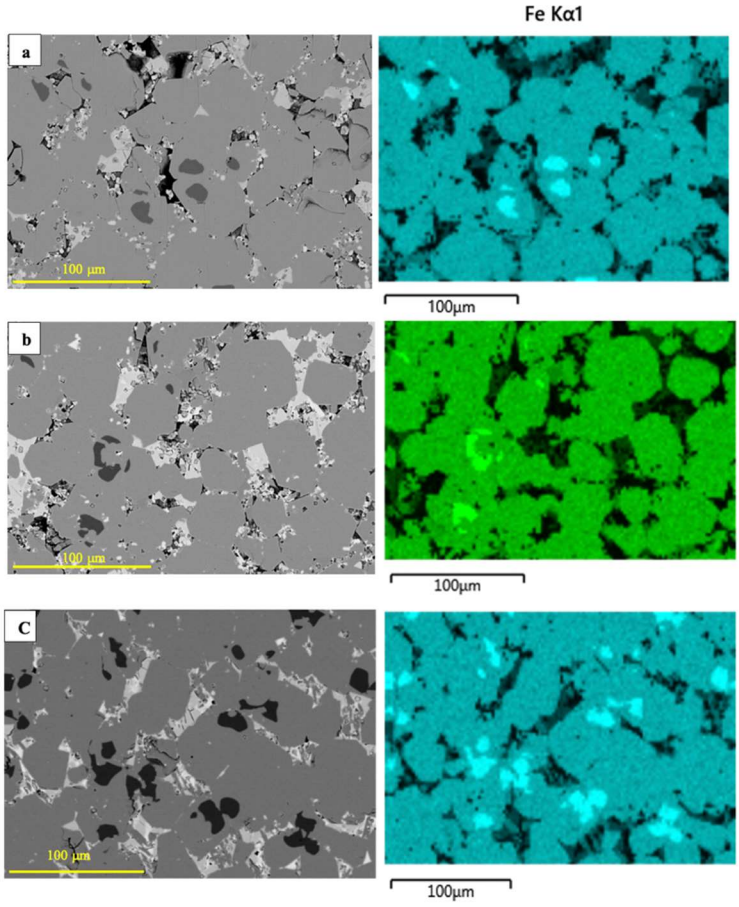

Figure 4.3 BSE image and Fe mapping of MM100 sample sintered at 1080 C with a. 7.5% b. 10% and c. 0% PrCu additives.

La concentration increased when MM substitution for Nd increased from 30 to 60% and remains almost same in MM100 sample. This is due to the unstable nature of $La_2Fe_{14}B$ compound. It forms Fe and La-B compounds. The $La_2Fe_{14}B$ compound is unstable, difficult to obtain, being prone to strong segregations of α-Fe and La-B in both as-cast and melt-spun form [46]. Having a larger atomic radius, La has limited solubility in the $Nd_2Fe_{14}B$ phase so it is expected to be expelled to the grain boundaries. Such segregation behavior is confirmed from the microstructure of MM100 sample. Three samples were prepared with MM100 composition – MM100 with 7.5% PrCu addition sintered at 1080 °C for 1.5 hours, MM 100 with 10% PrCu sintered at 1080 °C for 1.5 hours, and MM100 without any PrCu addition sintered at 1080 °C for 1.5 hours (Figure 4.3 a, b, and c respectively).

Fe segregation is observed in all these sintered magnets (Dark gray contrast in SEM images in Figure 4.4). Fe segregation is more prevalent in the sample without any PrCu addition (Figure 4.4 c). This can be explained by the presence of more Fe and also Pr is not available to form 2:14:1 phase. Soft magnetic phases like Fe will deteriorate the intrinsic coercivity and maximum energy product of the magnets which are shown in the next section.

Hysteresis Characteristics and Magnetic Properties

Table 4.1 contains room temperature magnetic properties of MM substituted Nd-Fe-B sintered magnets. All the samples are strip-casted, hydrogen decrepitated, milled, sintered, and annealed under same conditions. In Figure 4.5 (BH)max as a function of mischmetal content in the alloy is plotted. From this plot it is evident that maximum energy product decreased monotonically with increase in MM content. The decline was rapid after 60 wt% substitution of MM for Nd and the (BH)max of MM100 sample is only 0.73 MG.Oe.

Table 4.1 Magnetic properties of MM+7.5%PrCu samples sintered at 1080 °C.

	Br (KG)	**Hcj (KOe)**	**BHmax (MG.Oe)**
MM0	11.51	6.58	29.39
MM20	11.46	6.47	28.65
MM30	11.15	6.36	24.89
MM40	10.21	6.94	21.87
MM50	11.45	5.04	21.65
MM60	9.45	6.75	18.88
MM70	10.04	3.46	14
MM100	5.73	0.49	0.73

As explained in the previous sections, Ce and La concentration in matrix phase increased with MM content and hence (BH)max is lowered due to the inferior magnetic properties of La/Ce2Fe14B compounds.

Also in Figure 4.5, coercivity, and remanence as a function of MM content in rare-earth elements present in the base alloy are shown. The overall trend of room temperature magnetic properties suggests a linear decline in properties as MM content in the alloy increases. However, the coercivity of MM40 and MM60 samples strayed away from the expected trend. For these two compositions, coercivity increased from what we would expect from the trend. This is because, for magnets with higher amounts of MM, besides the influence of the deterioration of Ha, we should consider the impact of grain boundary modification on the coercivity. Due to limited solubility of Ce and La in 2:14:1 phase, they tend to expel from the matrix phase and aggregate along the grain boundary forming thick intergranular phases. The influence of grain boundary

modification to some extent compensates for the effect of lower anisotropic field. However, the deteriorating anisotropic field at higher MM content weakens the effect of the modification of grain boundary. Therefore, the coercivity decreases again with further increasing in MM content.

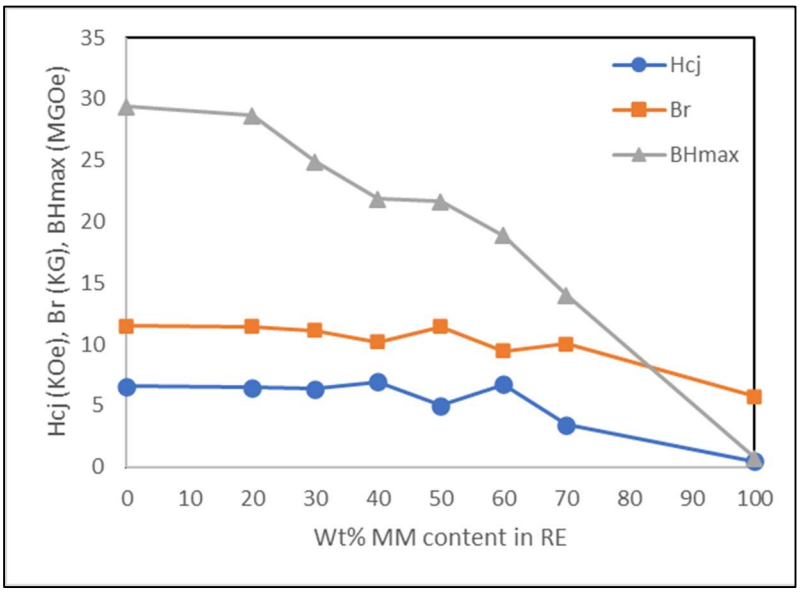

Figure 4.5 Magnetic Properties of MM Substituted Nd-Fe-B Magnets Sintered at 1080 °C.

One possible explanation for higher coercivity than expected for MM40 and MM60 magnets is that the post sintering conditions used are optimum for these two compositions. This implies that each composition has a different optimum annealing temperature that improves coercivity. No such deviations in coercivity are observed in samples that were sintered at 1060 °C (Figure 4.7)

Reduction in magnetic properties with MM substitution is due to the poor intrinsic properties of $MM_2Fe_{14}B$ and also due to the extrinsic features like microstructure. As shown in above section, grain coarsening is observed at higher MM substituted samples and Fe segregation in MM100 sample which resulted in extremely poor magnetic properties of MM100 alloys.

S1060

The microstructure of three samples - MM30 and MM40 and MM50 are shown in Figure 4.6. All these samples have similar grain size, and shape and grain size distribution in these samples is not uniform. Increasing the MM substitution for Nd from 30% to 50% did not induce any significant grain coarsening. SEM image on the right and left columns (Figure 4.6) were taken from the same area of the sample but at different magnifications.

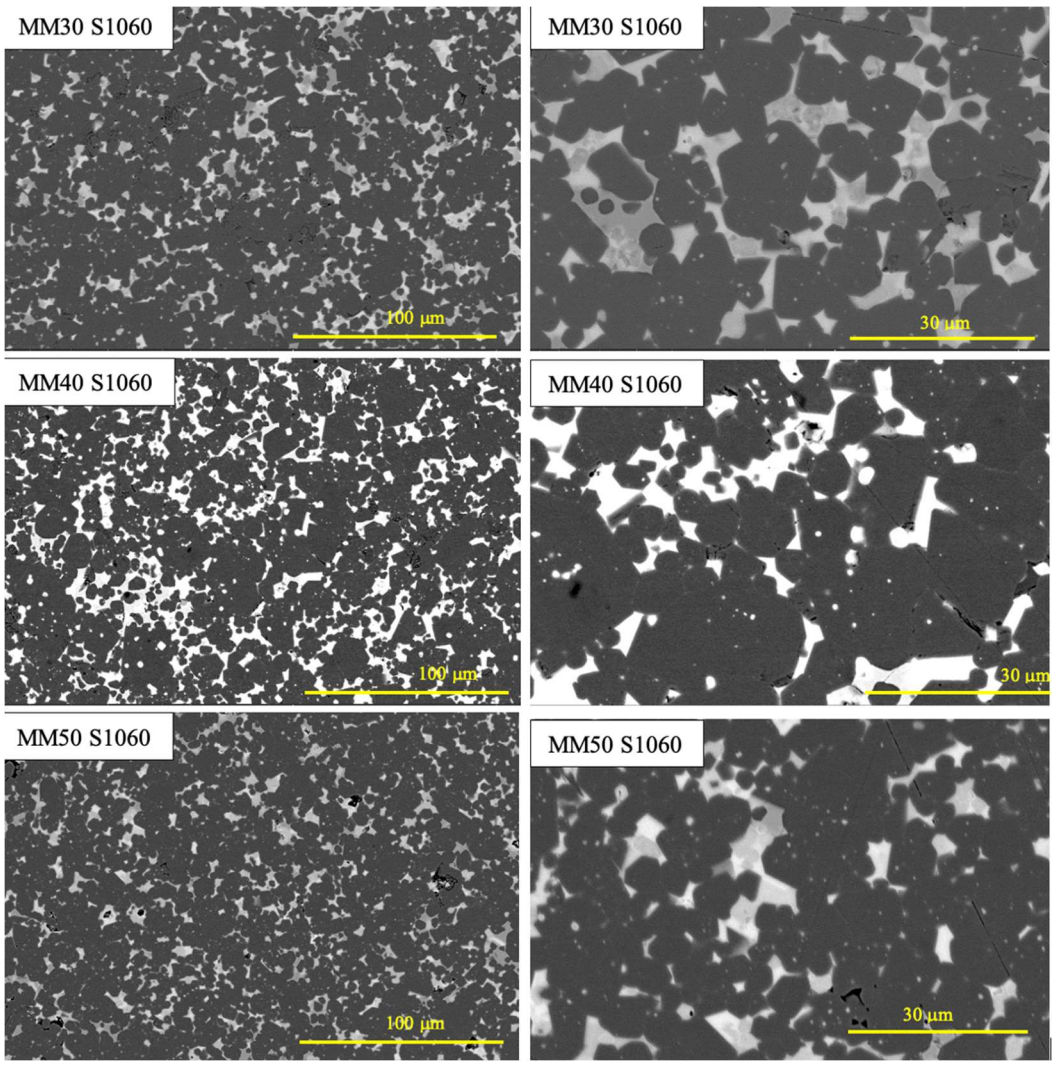

Figure 4.6 BSE Images of MM30, MM40 and MM50 Samples Sintered at 1060 °C for 3h (Left and Right-Side Images are taken at 500X and 1500x Magnification Respectively)

The presence of some very fine grains and some coarse grains is evident from the images taken at higher magnifications indicating a non-uniform grain distribution and similar morphology is also observed in the samples that are sintered at 1080 °C.

Room temperature magnetic properties of MM substituted samples are summarized inTable 4.2. For a given composition, samples sintered at 1060 °C have superior magnetic properties than those sintered at relatively higher temperature and shorter holding time. Properties of these magnets relating to microstructure are explained in the following sections. Of all the magnets prepared in this study, MM40 sample sintered at 1060 °C for 3 hours has the highest maximum energy product, 33.26 MG.Oe.

Table 4.2 Magnetic properties of MM+7.5%PrCu samples sintered at 1060 °C.

	Br (KG)	**Hcj (KOe)**	**(BH)max (MG.Oe)**
MM0	11.46	8.34	30.76
MM20	11.18	7.94	28.27
MM30	11.48	7.9	30.15
MM40	12.07	7.64	33.26
MM50	11.14	7.29	28.24
MM60	11.9	5.2	27.77

Figure 4.7 shows coercivity of samples sintered at 1060 °C as a function of MM substitution. With increasing MM content, monotonic decrease in coercivity is observed and it declined rapidly after 50% of Nd is substituted by MM.

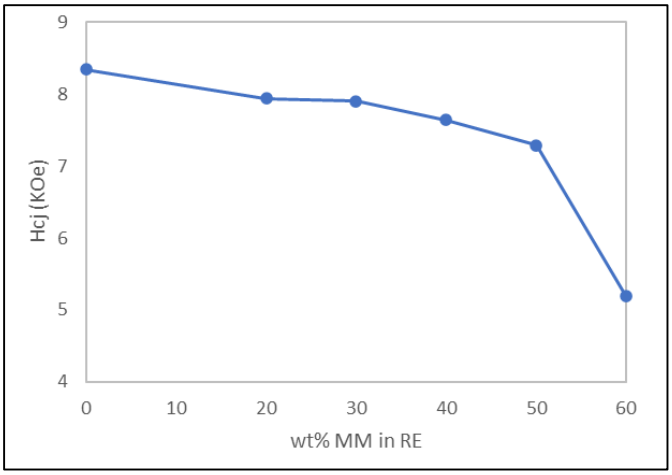

Figure 4.7 Coercivity of MM Substituted Nd-Fe-B Magnets Sintered at 1060 °C.

Squareness

Squareness factor (Q) of the demagnetization curve characterizes the magnetic stability of a magnet. Squareness close to 1 is preferred for magnet application. It is defined as the ratio of field at 90% remanence in the second quadrant of hysteresis loop to coercivity.

$$Q = \frac{H_{knee}}{H_{cj}}$$

Demagnetization of curves of three samples MM30, MM40 and MM50 sintered at 1060 °C were shown in Figure 4.8 and squareness factor calculated from these curves is summarized in the Table 4.3 along with other room temperature magnetic properties. Squareness of the magnets improved at higher MM substitution. Though the increment is not very significant, MM50 sample has better squareness,79%, than MM30 sample which has 75% squareness.

The increased squareness with increased MM content can be attributed to the low melting characters of La and Ce-enriched intergranular phase that helps to improve wettability between

the grain boundary and 2:14:1 main phase grains. The rare-earth rich grain boundary layer appearing along the grain boundaries is helpful to weaken the exchange coupling interactions between adjacent 2:14:1 grains and prevent the rapid propagations of reversal domains during the demagnetization process.

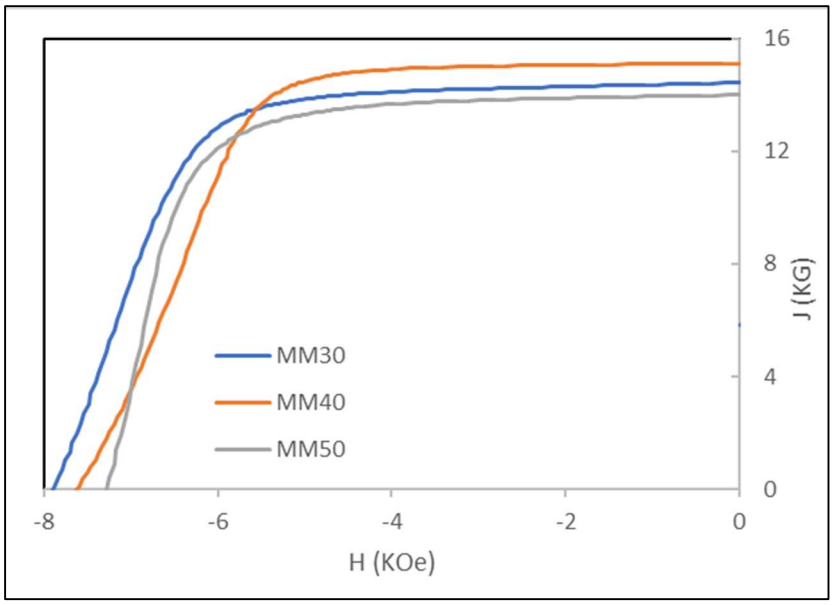

Figure 4.8 Demagnetization Curves of MM Samples Sintered at 1060 °C.

Table 4.3 Room Temperature Magnetic Properties of MM Magnets Sintered at 1060 °C for 3h.

	Max J (KG)	**Br (KG)**	**Hcj KOe**	**(BH)max (MG.Oe)**	**Squareness (%)**	**Density (g/cc)**
MM30	11.79	11.48	7.9	30.15	75.2	7.63
MM40	12.34	12.07	7.64	32.26	72.3	7.63
MM50	11.55	11.14	7.29	28.24	78.8	7.36

Effect of Sintering Temperature

The magnets are sintered at standard sintering conditions of NdFeB magnets which is 1080 °C for 1.5 hours. The samples reached full densification at this temperature. However, grain boundary distribution is not continuous in these samples. Hence holding time must increase. Therefore, the holding time is increased from 1.5 hours to 3 hours so that liquidus phase has enough time to surround the main phase. However, longer holding times at higher temperature might lead to grain coarsening. Therefore, sintering was lowered to 1060 °C.

Magnetic Properties

Table 4.4 and Table 4.5 contains the magnetic properties of MM substituted samples sintered at different conditions. Remanence, coercivity, and maximum energy product improved in both samples that were sintered at 1060 °C for 3 hours compared to those that are sintered at 1080 °C for 1.5 hours. Coercivity is increased by 24.2%, 9.8%, and 30.9% respectively for MM30, MM40 and MM50 samples when sintered at 1060 °C. The improvement in magnetic properties can be explained in terms of microstructure.

Table 4.4 Room Temperature Magnetic Properties of MM30 Samples Sintered at 1080 °C and 1060 °C.

Sintering Temperature (°C)	**Br (KG)**	**Hcj (KOe)**	**BHmax (MG.Oe)**
1080	11.15	6.36	24.89
1060	11.48	7.9	30.15

Table 4.5 Room Temperature Magnetic Properties of MM40 Samples Sintered at 1080 °C and 1060 °C.

Sintering Temperature (°C)	**Br (KG)**	**Hcj (KOe)**	**(BH)max (MGOe)**
1080	10.21	6.94	21.87
1060	12.03	7.62	32.88

Microstructure

After sintering at 1060 °C, continuous grain boundaries are formed between as shown in Figure 4.9. In this figure, the back scattered electron images on the left belong to the samples that are sintered at 1080 °C and images on the right are taken from the samples sintered at 1060 °C having same composition as their respective left images. Absence of secondary phases in some regions is evident from the MM30 sample sintered at 1080 °C which explains the enhancement in coercivity in the sample having same composition but sintered at lower temperature for longer holding time. It is worth noting that sintering conditions significantly influence the wetting behavior of the grain boundary phases and triple junctions. The density was not significanlty changed when the sintering temperature increased from 1060 to 1080 °C indicating that full densification was achieved even at 1060 °C.

From microstructure analysis, there is no significant difference in grain size, and grain size distribution with change in sintering temperature. Since there is no grain coarsening at higher temperatures, formation of continuous grain boundaries can be attributed to the longer holding time, 3 hours, at 1060 °C.

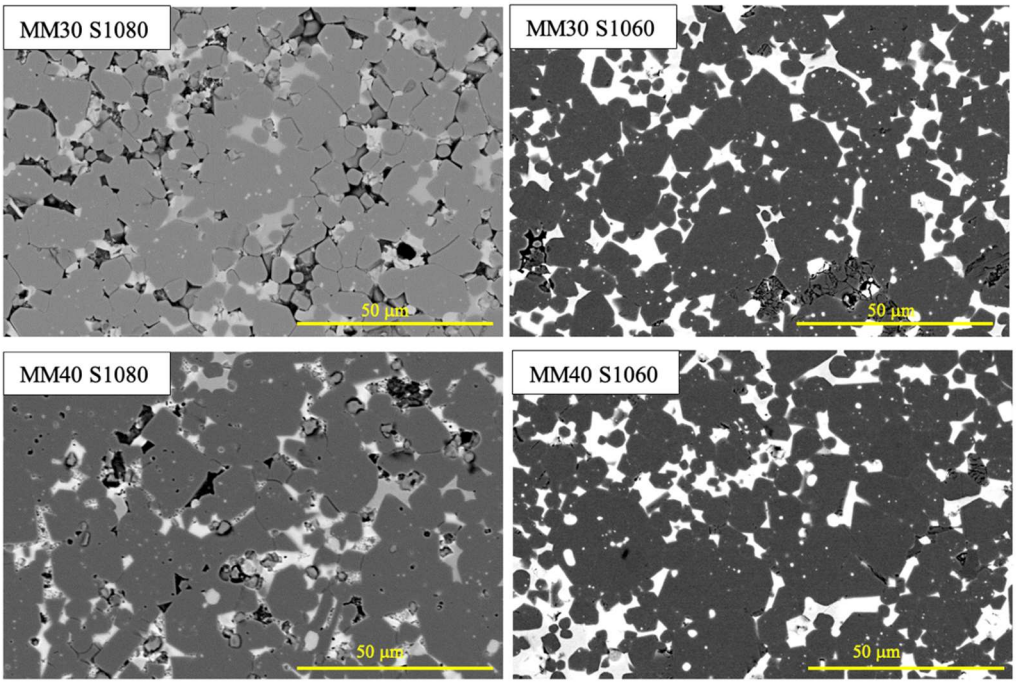

Figure 4.9 Microstructure Comparison of MM30 and MM40 Samples Sintered at Different Temperatures.

Continuous grain boundaries can be further seen from EDS elemental maps. In Figure 4.10, the SEM image on the top row is from MM30 sample sintered at 1060 °C, and the corresponding colored images show the mapping of Cu and other rare earth elements. Similarly, the bottom row images show the elemental mapping of sample having same composition as MM30 but sintered at 1080 °C. In maps, the color of an image is brighter if the content of the corresponding element is high in the regions, whereas the darker color indicates the absence or very poor concentration of elements in those regions. The intergranular phase is much brighter showing continuous network like grain boundaries in the sample sintered at 1060 °C.

From the elemental mappings in bottom row, though rare earth rich phases are present across the grain boundaries, distribution is not continuous and absent in some regions.

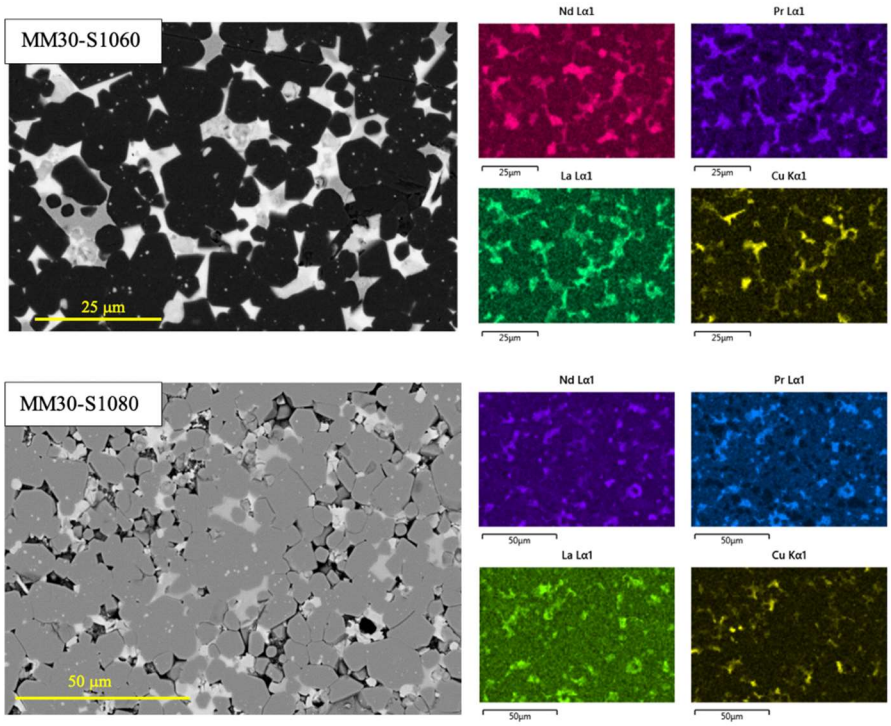

Figure 4.10 EDS Elemental Mapping Showing Nd, Pr, La and Cu in Grain Boundary Regions and Triple Junctions of MM30 sample.

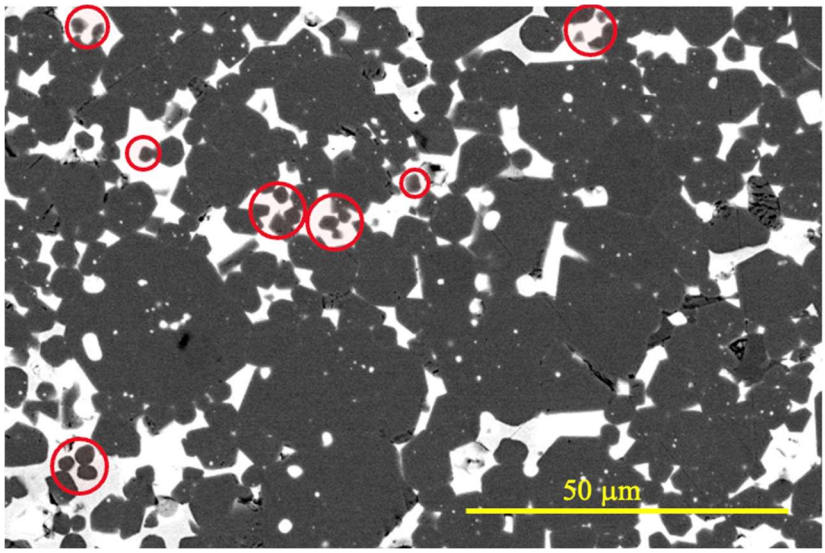

Figure 4.11 SEM Image of MM40 S1060 Sample Showing the Presence of Various Fine Grains.

Remanence depends on, degree of alignment of the C-axis, density, and volume fraction of the main phase grains. Lower remanence at higher sintering temperature can be due to change in orientation of some small main phase grains as they might dissolve in liquid phase at higher temperatures. Very fine grains are highlighted in Figure 4.11 whereas such small grains are absent in the sample sintered at higher temperature. Low coercivity due to lower holding times coupled with low remanence due to high temperature decreases the maximum energy product of magnets sintered at 1080 °C for 1.5 hours.

Effect of PrCu Addition

Microstructure

MM substituted magnets without PrCu additives were prepared to study the influence of PrCu additives on microstructure and magnetic properties of MM magnets. Microstructure of MM70 samples with and without PrCu addition in different regions are shown in Figure 4.12.

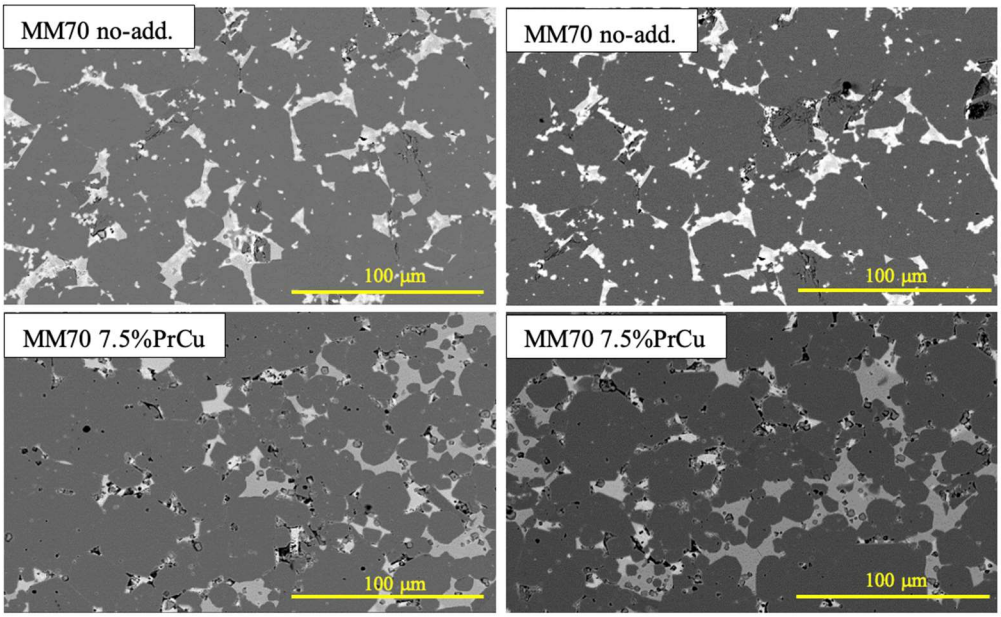

Figure 4.12 BSE Images of MM70 samples with 0% PrCu (Top) and 7.5% PrCu (Bottom) addition.

All the samples in Figure 4.12 have same base alloy composition and sintered under similar conditions. However, the sample on top row (both the SEM images on top row were taken from different areas of the same sample) had no additives whereas for the sample on the bottom row (both the SEM images on the bottom row were taken from different areas of the same sample) had 7.5 wt% PrCu was added to the base alloy. Relatively high-volume fraction of grain boundary phases is evident in sample with PrCu. In sample without PrCu additives, the interface between matrix phases is not well defined and neighboring grains are in direct contact without any rare-earth rich grain boundaries in between. This drastically reduces coercivity as due to direct contact between the matrix grains, reverse magnetic domains rapidly propagate, and this behavior is reflected in the coercivity of these samples which is shown in the table.

Though both these samples have comparable grain size, the distribution of grains is not uniform in the sample that has PrCu. Grain refinement with PrCu addition is evident from SEM images. At 7.5 wt% PrCu, the grain size distribution is non-uniform, with fine grains of diameters as small as 3 μm are present. While in the PrCu free sample, the grain size distribution is more uniform, but it contains coarse grains with average grain size of 21 μm.

Table 4.6 Room Temperature Magnetic Properties of MM70 Sample with Different PrCu Content Sintered at 1080 °C.

Wt% PrCu	**Max J (KG)**	**Br (KG)**	**Hcj (KOe)**	**BHmax (MG.Oe)**
0	11.38	3.29	0.22	0.17
7.5	10.56	10.04	3.46	14

One of the explanations for significantly low coercivity in PrCu free samples is not using optimum annealing temperature. Tang et.al, [51] reported that high temperature annealing has no influence on 5 wt% and 10 wt% PrCu added samples. However, samples without any PrCu

additives show positive coercivity effects at high temperature annealing at 900 °C and negative coercivity effects at low temperature annealing. Pr replaces Ce in the 2:14:1 which has higher anisotropic field (Table 2.1). Grain refinement coupled with continuous grain boundary formation with addition of PrCu improves the coercivity.

PrCu distribution

To understand the distribution of PrCu in these alloys, EDS elemental mappings of Pr and Cu (Figure 4.13) were studied. In these maps, Cu and Pr are brighter in the regions where SEM image shows bright contrast indicating intergranular regions. We can conclude that Pr and Cu are going into the grain boundary regions thereby increasing the volume fractions of the intergranular phases.

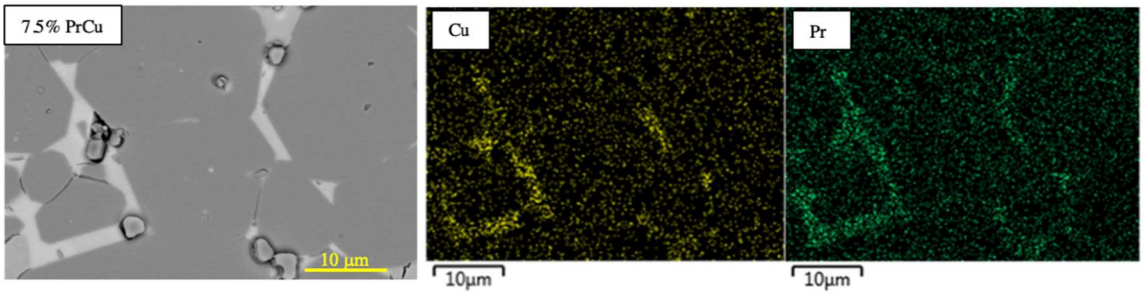

Figure 4.13 Microstructure with Cu and Pr Maps of MM70 S1080 Sample.

Grain size

To investigate the distribution of Pr in the sample, composition analysis is given in Table 4.7 which contains element distribution of various main phase grains. Grains of different sizes (Figure 4.14) were selected to esatblish a relation between grain size and the amount of Pr in that grain.

From Table 4.7 we can conclude that, Pr content is higher for the grains having smaller average grain diameters meaning PrCu rich regions restricted the grain growth and Pr from the

grain boundary regions diffused into the matrix grains thereby enhancing the local anisotropy. This explains non-uniform grain size distribution in samples with PrCu additives.

Table 4.7 Average Grain Diameter of Different Matrix Grains with Spectrum Labels Shown in Figure 4.14.

Sprectrum Label	Average grain diameter (μm)	Fe	Co	Nd	Pr	Ce	La
1	7.04	72.5	11	7.8	0.7	3.2	1.4
2	3.25	72.1	11.2	7.5	1.1	3.1	1.4
3	1.52	71.6	11.1	7.0	2.2	2.9	1.4
4	1.16	67	10.6	7.3	2.7	3.1	1.5

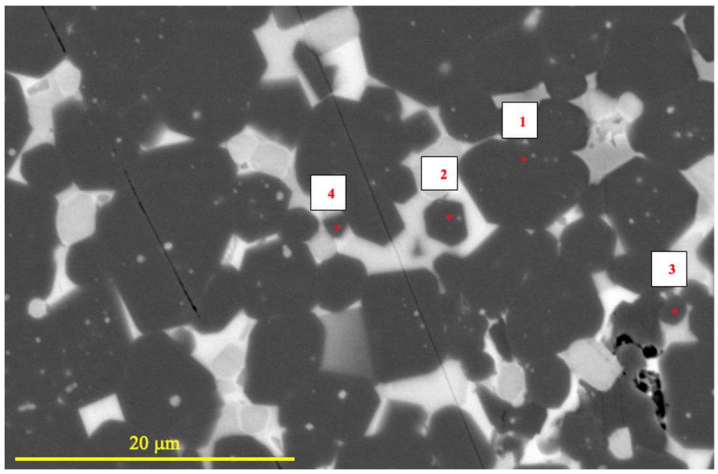

Figure 4.14 Spectrum Labels Correspond to Table 4.7

Grain Boundary Phases

PrCu led to the formation of additional grain boundary phases than one would see in conventional sintered NdFeB magnets. Four major grain boundary phases are identified which

are shown below – 1.RE(Nd,Pr,La)-Cu rich, 2.RE(Nd,Pr,Ce,La)oxide, 3. RE-Fe-Ga-Cu, and 4. Fe-Co-Ce rich.

Grain boundary phases with bright contrast in Figure 4.15 are RE(Nd,Pr,La)-Cu rich. Continuous network of such Cu-enriched layers can be seen throughout the microstructure.

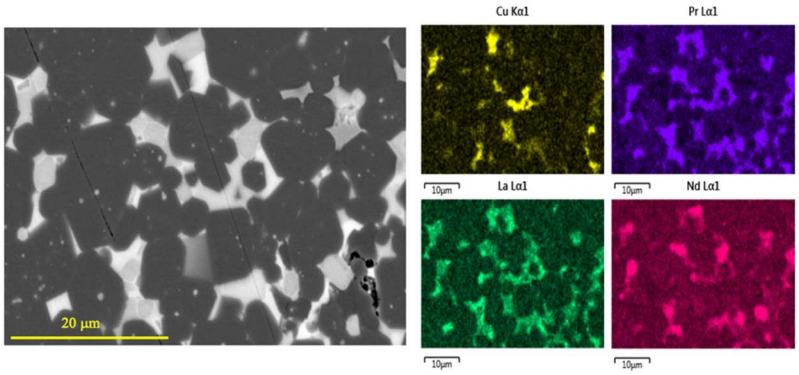

Figure 4.15 BSE Image and EDS Elemental Mapping of MM50 S1060 Sample.

The larger, more rounded RE-rich grains with light gray contrast are oxides which are highlighted in Figure 4.16. The mean size of these grains is 2 µm. The nature of these oxide phases present at the interface may have an important impact on coercivity.

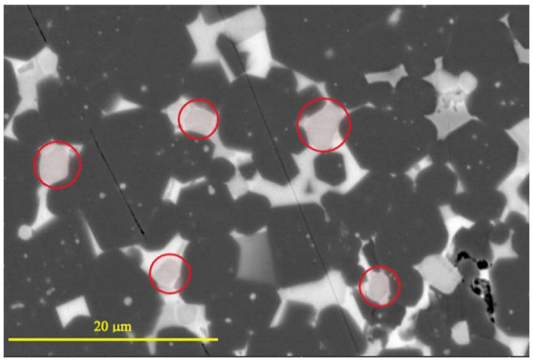

Figure 4.16 BSE Image Of MM50 Sample Sintered At 1060 °C with Red Circles Indicating RE-Oxide Phases.

From EDS point analysis shown in Table 4.8, these phases can be NdO (RE) which has FCC crystal structure. The presence of RE-rich oxides introduces distortions to the $Re_2Fe_{14}B$ unit

cell. The distortions at the interface between $Re_2Fe_{14}B$ and REO are detrimental to the coercivity as the distorted regions have reduced magneto-crystalline anisotropy.

Table 4.8 Composition of Circles Marked in Figure 4.16 in Atom%.

O	Nd	Pr	Ce	La
44.7	25.2	12.3	7.3	7.1
50.3	23.8	10.6	6.9	6.4
48.2	24.4	11.4	7.1	6.7
49.5	23.7	11.3	6.7	6.5
47.3	24.5	11.5	7.0	6.9

In Figure 4.17, the two regions marked correspond to RE-Fe-Co-Cu-Ga phases. In these regions, the grain boundary from triple junctions infiltrate into grain bounaries forming a realtively thin layers betwen the matrix phase grains.

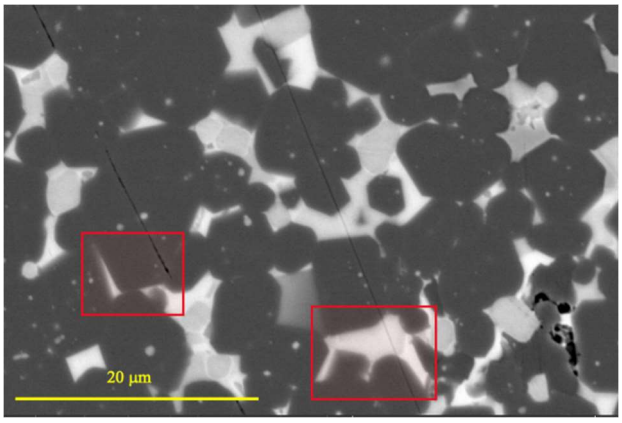

Figure 4.17 BSE Image Of MM50 S1060 Magnet with Red Boxes Indicating RE-Fe-Co-Cu-Ga Phases.

Cu is known to decrease the melting point of Nd-rich phases thereby improving the wettability of liquid RE rich phases during annealing and therefore these phases are drawn into

the grain boundaries. Ga also has been shown to enhance the wettability of the grain boundaries [57]. Similar effect is shown in MM sample sintered at 1080 °C.

Regions indicated by red dots in Figure 4.18 are Fe-Co-Ce rich. Presence of Fe at grain boundaries is not preferred as if there are ferromagnetic phases between matrix grains, once reverse domains nucleate at defects/sharp edges, the reverse magnetization continues simply by reverse domain expansion due to the exchange interaction.

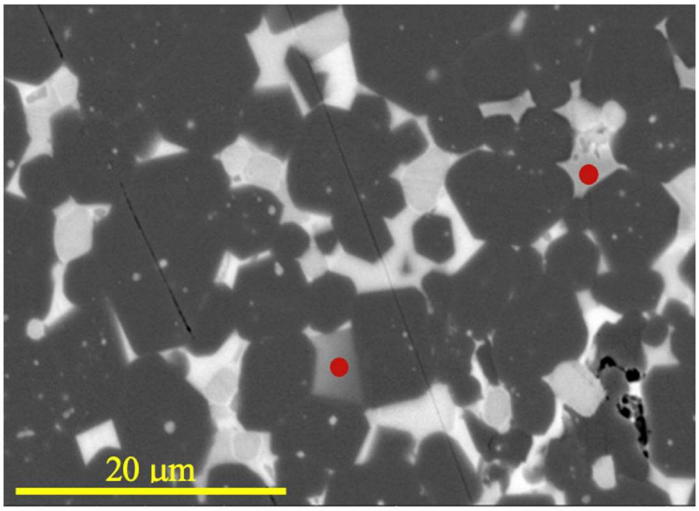

Figure 4.18 BSE Image Of MM50 S1060 Magnet with Red Dots Indicating Fe-Co-Ce Rich Phases

High Tempetature Measurements

Magnetic properties at elevated temperatures of MM30 and MM40 samples sintered at 1060 °C were measured using Vibrating Sample Magnetometer (VSM). Figure 4.19 shows the coercivity of MM30 and MM40 magnets as a function of temperature and Table 4.9 contains the temperature coefficient values of intrinsic coercivity (β) which is calculated using the formula below –

$$\beta = \frac{Hcj\ (300K) - Hcj\ (400K)}{Hcj\ (300K) \times (300K - 400K)} \times 100$$

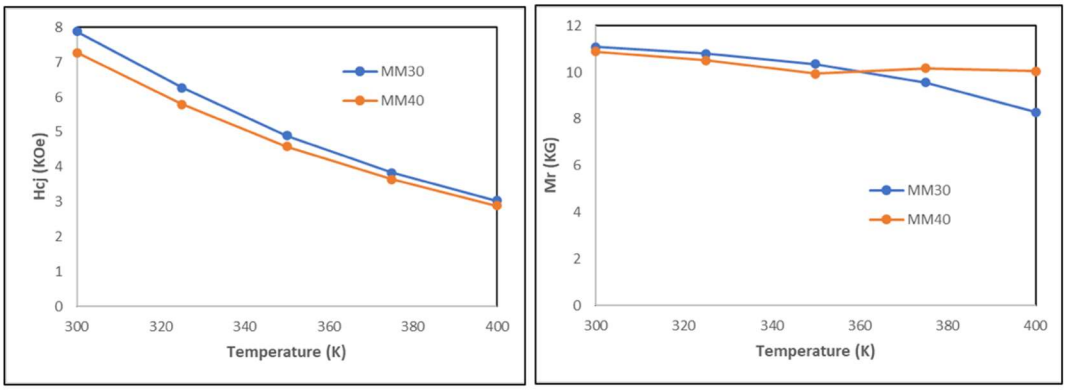

Figure 4.19 Coercivity and Remanence as a Function of Temperature

The absolute value of β (|β|) is slightly lower for MM40 sample as compared to MM30. The change of β has a relationship with temperature dependence of intrinsic properties such as magnetization and magneto-crystalline anisotropy of matrix phase and the microstructure of magnet. Because the temperature dependence of anisotropic field for $Ce_2Fe_{14}B$ is weaker than that of $Nd_2Fe_{14}B$ and $Pr_2Fe_{14}B$, and the microstructure is modified, these factors have positive effect on the temperature coefficient of coercivity of MM40 sample.

Table 4.9 Temperature Coefficient of Intrinsic Coercivity of Samples with Different MM Content

Sample	**$\beta_{300\text{-}400K}$ (%/K)**
MM30	-0.62
MM40	-0.60

CHAPTER 5. SUMMARY & CONCLUSION

To address criticality of the rare-earth elements used in permanent magnet manufacturing, we studied the utilization of Mischmetal to partially substitute Nd in $Nd_2Fe_{14}B$ sintered permanent magnets. MM can be a potential substitute as it is cheap and using MM reduces the imbalanced use of rare-earth elements. This thesis contains experimental research data relating composition, microstructure, and magnetic properties of MM substituted $Nd_2Fe_{14}B$ alloys. The influence of the alloy composition and sintering temperature on microstructure and resulting magnetic properties were analyzed for the sintered magnets using various techniques like XRD, SEM, EDS, VSM, and magnetic hysteresisgrapher.

First, MM is substituted in the alloy having nominal composition $(Nd_{1-x}MM_x)_{2.64}Fe_{12}Co_2B_{1.06}$ for x = 0, 0.2 ,0.3, 0.4, 0.5, 0.6, 0.7, and1. All these alloys were produced by strip casting and added with 7.5 wt% PrCu and sintered at the standard sintering conditions of Nd-Fe-B based alloys, 1080 °C for 1.5 hours. SEM analysis showed that grain coarsening is induced with increase in MM content. The overall trend shows that room temperature magnetic properties deteriorate with increase in MM content. However, alloys with x = 0.4 and 0.6 composition have better coercivity and lower remanence than what is expected from the trend. Post-sintering annealing conditions are the same for all the samples. This deviation forms the trend can be due to processing conditions like disturbance in alignment, oxygen contamination or the sintering and annealing temperature is optimum for that particular composition. The maximum energy product of the magnets decreased with increasing MM content with a rapid drop after x = 0.7. Fe is segregated in x = 1 sample which explains the very poor coercivity of this alloy as soft magnetic phases like α-Fe are detrimental to hard magnetic properties.

For the second batch of samples, PrCu was not added to the base alloy to study the influence of eutectic non-magnetic alloys on the coercivity of MM substituted Nd-Fe-B alloys. SEM results clearly indicated grain refinement to some extent when PrCu is added to the samples. Sintering and post-sintering annealing conditions were studied for both batches. The low temperature annealing employed for the samples might not be optimum for the samples without PrCu addition. Cu decreases the melting point of Nd-rich phases and hence low temperature heat treatment is beneficial for the formation of continuous grain boundaries when PrCu is added. However, it is reported in literature that such annealing conditions are detrimental to Nd-Fe-B alloys when no eutectic additives are added. High annealing temperature at ~900 °C probably improves the coercivity of samples from the second batch.

The third batch of samples were prepared using the same composition as the first batch. However, different sintering conditions were used to study the effect of holding time and sintering temperature on resulting microstructure and magnetic properties. Samples were sintered at 1060 °C for 3 hours. Room temperature magnetic properties are improved for samples sintered at 1060 °C. Continuous grain boundary networks are evident from SEM BSE images and EDS elemental mapping. No significant grain coarsening is observed in samples sintered at 1080 °C with respect to those sintered at 1060 °C. Therefore, high coercivity in samples sintered at 1060 °C can be attributed to longer holding time which facilitates the formation of continuous intergranular phases thereby proving magnetic isolation to $MM_2Fe_{14}B$ grains and also promotes the solid-state diffusion of Pr from PrCu to replace Ce/La in $(CeLa)_2Fe_{14}B$ phase thereby forming higher local anisotropy regions on the surface. (BH)max is increased by about 50% in MM40 sample sintered at 1060 °C as compared to that sintered at 1080 °C.

In conclusion, a maximum energy product as high as 30 MGOe can be obtained in a Nd-Fe-B sintered magnet having 50 wt% MM in rare-earth content. By optimizing sintering and post-sintering conditions, and the amount of PrCu, the magnetic properties can be further improved. This work might open potential interesting paths for further research in the development of critical rare-earth lean or free permanent magnets.

REFERENCES

Croat, John J., Jan F. Herbst, Robert W. Lee, and Frederick E. Pinkerton. "Pr-Fe and Nd-Fe-based materials: A new class of high-performance permanent magnets." *Journal of Applied Physics* 55, no. 6 (1984): 2078-2082.

Sagawa, Masato, Setsuo Fujimura, Norio Togawa, Hitoshi Yamamoto, and Yutaka Matsuura. "New material for permanent magnets on a base of Nd and Fe." *Journal of Applied Physics* 55, no. 6 (1984): 2083-2087.

Trout, S. "Rare-earth magnet industry in the USA: Current status and future trends." In *XVII Rare-earth Magnet Workshop, Newark, DE*. 2002.

Herbst, Jan F., John J. Croat, Frederick E. Pinkerton, and W. B. Yelon. "Relationships between crystal structure and magnetic properties in Nd 2 Fe 14 B." *Physical Review B* 29, no. 7 (1984): 4176.

Brown, David, Bao-Min Ma, and Zhongmin Chen. "Developments in the processing and properties of NdFeb-type permanent magnets." *Journal of magnetism and magnetic materials* 248, no. 3 (2002): 432-440.

Calin, Marius-Daniel, and Elena Helerea. "Temperature influence on magnetic characteristics of NdFeB permanent magnets." In *2011 7th international symposium on advanced topics in electrical engineering (ATEE)*, pp. 1-6. IEEE, 2011.

Gutfleisch, Oliver, Matthew A. Willard, Ekkes Brück, Christina H. Chen, S. G. Sankar, and J. Ping Liu. "Magnetic materials and devices for the 21st century: stronger, lighter, and more energy efficient." *Advanced materials* 23, no. 7 (2011): 821-842.

Bai, G., R. W. Gao, Y. Sun, G. B. Han, and B. Wang. "Study of high-coercivity sintered NdFeB magnets." *Journal of magnetism and magnetic materials* 308, no. 1 (2007): 20-23.

United States Department of Energy, "2011 Critical Materials Strategy," 2011. https://www.energy.gov/sites/default/files/DOE_CMS_2011_Summary.pdf.

Senate Commitee on Energy and Natural Resources, "Projected Demand for Critical Minerals Used in Solar and Wind Energy Systems and," 10 September 2019. https://www.energy.senate.gov/services/files/28F0D27F-BC97-4D06-997C-0CE6FD5760C4.

P. Falconnet, "The economics of rare-earths," *Journal of the Less Common Metals,* vol. 111, no. 1-2, pp. 9-15, 1985.

Binnemans, Koen, Peter Tom Jones, Karel Van Acker, Bart Blanpain, Brajendra Mishra, and Diran Apelian. "Rare-earth economics: the balance problem." *Jom* 65 (2013): 846-848.

Tang, Wei, Gaoyuan Ouyang, Jing Wang, Harika Dasari, Matthew J. Kramer, Iver E. Anderson, and Jun Cui. "Development of Dy-free Nd-Fe-B-based sintered magnet through grain boundary engineering using Pr-Cu alloys." *IEEE Transactions on Magnetics* (2023).

Cullity, Bernard Dennis, and Chad D. Graham. *Introduction to magnetic materials*. John Wiley & Sons, 2011.

Coey, John MD. *Magnetism and magnetic materials*. Cambridge university press, 2010.

Woodcock, T. G., Yuepeng Zhang, Gino Hrkac, Georgeta Ciuta, N. M. Dempsey, T. Schrefl, Oliver Gutfleisch, and Dominique Givord. "Understanding the microstructure and coercivity of high performance NdFeB-based magnets." *Scripta Materialia* 67, no. 6 (2012): 536-541.

Ramesh, R., and K. Srikrishna. "Magnetization reversal in nucleation controlled magnets. I. Theory." *Journal of applied physics* 64, no. 11 (1988): 6406-6415..

Uestuener, K., M. Katter, and W. Rodewald. "Dependence of the mean grain size and coercivity of sintered Nd–Fe–B magnets on the initial powder particle size." *IEEE transactions on magnetics* 42, no. 10 (2006): 2897-2899.

Sepehri-Amin, H., T. Ohkubo, M. Gruber, T. Schrefl, and K. Hono. "Micromagnetic simulations on the grain size dependence of coercivity in anisotropic Nd–Fe–B sintered magnets." *Scripta Materialia* 89 (2014): 29-32.

Uestuener, K., M. Katter, and W. Rodewald. "Dependence of the mean grain size and coercivity of sintered Nd–Fe–B magnets on the initial powder particle size." *IEEE transactions on magnetics* 42, no. 10 (2006): 2897-2899.

Zhou, Qing, Wei Li, Yuan Hong, Lizhong Zhao, Xichun Zhong, Hongya Yu, Lili Huang, and Zhongwu Liu. "Microstructure improvement related coercivity enhancement for sintered NdFeB magnets after optimized additional heat treatment." *Journal of Rare-earths* 36, no. 4 (2018): 379-384.

Sepehri-Amin, H., T. Ohkubo, T. Shima, and K. Hono. "Grain boundary and interface chemistry of an Nd–Fe–B-based sintered magnet." *Acta Materialia* 60, no. 3 (2012): 819-830.

Herbst, J. F. "R 2 Fe 14 B materials: Intrinsic properties and technological aspects." *Reviews of Modern Physics* 63, no. 4 (1991): 819.

A. P. Bains, "Lanthanide Contraction-Chemistry LibreTexts," https://chem.libretexts.org/Bookshelves/Inorganic_Chemistry/Modules_and_Websites_(Inorganic_Chemistry)/Descriptive_Chemistry/Elements_Organized_by_Block/4_f_Block_Elements/The_Lanthanides/aLanthanides%3A_Properties_and_Reactions/Lanthanide_Contraction.

Herbst, J. F., and W. B. Yelon. "Crystal and magnetic structure of Ce2Fe14B and Lu2Fe14B." *Journal of magnetism and magnetic materials* 54 (1986): 570-572.

Slater, John C. "Cohesion in monovalent metals." *Physical Review* 35, no. 5 (1930): 509.

Slater, John C. "Atomic shielding constants." *Physical review* 36, no. 1 (1930): 57.

Matsuura, Yutaka, Satoshi Hirosawa, Hitoshi Yamamoto, Setsuo Fujimura, Masato Sagawa, and Kozo Osamura. "Phase diagram of the Nd-Fe-B ternary system." *Japanese journal of applied physics* 24, no. 8A (1985): L635.

Hono, K., and H. Sepehri-Amin. "Strategy for high-coercivity Nd–Fe–B magnets." *Scripta Materialia* 67, no. 6 (2012): 530-535.

Bernardi, J., J. Fidler, M. Sagawa, and Y. Hirose. "Microstructural analysis of strip cast Nd–Fe–B alloys for high (BH) max magnets." *Journal of applied physics* 83, no. 11 (1998): 6396-6398.

Yu, L. Q., M. Yan, J. M. Wu, W. Luo, X. G. Cui, and H. G. Ying. "On the cooling rate of strip cast ingots for sintered NdFeB magnets." *Physica B: Condensed Matter* 393, no. 1-2 (2007): 1-5.

Chen, Hao, Weiqiang Liu, Zhi Li, Yuqing Li, Yantao Yin, Haiyuan Cui, and Ming Yue. "Optimizing microstructure and magnetic properties of mischmetal-based sintered magnets by grain refinement." *Materials Letters* 267 (2020): 127509.

Harris, I. R., C. Noble, and T. Bailey. "The hydrogen decrepitation of an Ndi15Fe77B8 magnetic alloy." *Journal of the Less Common Metals* 106, no. 1 (1985): L1-L4.

Yartys, V. A., A. J. Williams, K. G. Knoch, P. J. McGuiness, and I. R. Harris. "Further studies of anisotropic hydrogen decrepitation in Nd16Fe76B8 sintered magnets." *Journal of Alloys and Compounds* 239, no. 1 (1996): 50-54.

Harris, I. R., J. Evans, and P. Nyholm. "British Patent 1554384." (1979).

McGuiness, Paul J., and I. R. Harris. "The use of hydrogen in the production and characterization of NdFeB magnets." *Journal of applied physics* 64, no. 10 (1988): 5308-5310.

Williams, A. J., Paul J. McGuiness, and I. R. Harris. "Mass spectrometer hydrogen desorption studies on some hydrided NdFeB-type alloys." *Journal of the Less Common Metals* 171, no. 1 (1991): 149-155.

J. Ormerod, "Magnetics Magazine," August 2016. https://magneticsmag.com/how-to-assure-every-rare-earth-or-any-magnet-meets-your-requirements-100-percent-of-the-time/.

Zhu, Minggang, Wei Li, Jingdai Wang, Liyun Zheng, Yanfeng Li, Ke Zhang, Haibo Feng, and Tao Liu. "Influence of Ce content on the rectangularity of demagnetization curves and magnetic properties of Re-Fe-B magnets sintered by double main phase alloy method." *IEEE transactions on magnetics* 50, no. 1 (2013): 1-4.

Zhang, Yujing, Tianyu Ma, Jiaying Jin, Jiangtao Li, Chen Wu, Baogen Shen, and Mi Yan. "Effects of REFe2 on microstructure and magnetic properties of Nd-Ce-Fe-B sintered magnets." *Acta Materialia* 128 (2017): 22-30.

Yan, Changjiang, Shuai Guo, Renjie Chen, Dong Lee, and Aru Yan. "Effect of Ce on the magnetic properties and microstructure of sintered didymium-Fe-B magnets." *IEEE Transactions on Magnetics* 50, no. 10 (2014): 1-5.

Chen, Hao, Yuqing Li, Hongguo Zhang, Weiqiang Liu, Haihui Wu, Yuan Qin, Ming Yue, Qifeng Wei, Baoguo Zhang, and Jinghui Di. "Strategy for Co-Enhancement of Remanence–Coercivity of RE-Fe-B Sintered Magnets with High Ce-Content: Appropriate La Substitution." *Advanced Science* (2023): 2301312.

Shi, Qi, Ying Liu, Jun Li, Wei Zhao, Renquan Wang, and Xi Gao. "Significant improvement of the 2: 14: 1 phase formability and magnetic properties of multi-phases RE-Fe-B magnets with La substitution for Ce." *Journal of Magnetism and Magnetic Materials* 476 (2019): 1-6.

Liao, X. F., J. S. Zhang, H. Y. Yu, X. C. Zhong, L. Z. Zhao, K. Xu, D. R. Peng, and Z. W. Liu. "Maximizing the hard magnetic properties of melt-spun Ce–La–Fe–B alloys." *Journal of Materials Science* 54, no. 9 (2019): 7288-7299.

Zhang, Z. Y., L. Z. Zhao, J. S. Zhang, X. C. Zhong, W. Q. Qiu, D. L. Jiao, and Z. W. Liu. "Phase precipitation behavior of rapidly quenched ternary La–Fe–B alloy and the effects of Nd substitution." *Materials Research Express* 4, no. 8 (2017): 086503.

Hadjipanayis, G. C., Y. F. Tao, and K. Gudimetta. "Formation of Fe14La2B phase in as-cast and melt-spun samples." *Applied physics letters* 47, no. 7 (1985): 757-758.

Tang, Minghui, Xiaoqian Bao, Yishui Zhou, Kechao Lu, Jiheng Li, and Xuexu Gao. "Microstructure and annealing effects of NdFeB sintered magnets with Pr-Cu boundary addition." *Journal of Magnetism and Magnetic Materials* 505 (2020): 166749.

Tang, Minghui, Xiaoqian Bao, Kechao Lu, Lu Sun, Jiheng Li, and Xuexu Gao. "Boundary structure modification and magnetic properties enhancement of Nd–Fe–B sintered magnets by diffusing (PrDy)–Cu alloy." *Scripta Materialia* 117 (2016): 60-63.

Wan, Fangming, Yinfeng Zhang, Jingzhi Han, Shunquan Liu, Tao Liu, Lei Zhou, Jianbo Fu et al. "Coercivity enhancement in Dy-free Nd–Fe–B sintered magnets by using Pr-Cu alloy." *Journal of applied physics* 115, no. 20 (2014).

Liu, Weiqiang, Zhipeng Zhang, Ming Yue, Zhi Li, Dan Wu, Zhao Zhou, Hao Chen, Yuqing Li, Zaisheng Pang, and Xi Yu. "MM-Fe-B based gap magnet with excellent energy density." *Intermetallics* 115 (2019): 106626.

Shang, R. X., J. F. Xiong, R. Li, W. L. Zuo, J. Zhang, T. Y. Zhao, R. J. Chen, J. R. Sun, and B. G. Shen. "Structure and properties of sintered MM–Fe–B magnets." *AIP Advances* 7, no. 5 (2017).

Xiong, Jie-Fu, Rong-Xiang Shang, Yan-Li Liu, Xin Zhao, Wen-Liang Zuo, Feng-Xia Hu, Ji-Rong Sun, Tong-Yun Zhao, Ren-Jie Chen, and Bao-Gen Shen. "Magnetic properties of misch-metal partially substituted Nd–Fe–B magnets sintered by dual alloy method." *Chinese Physics B* 27, no. 7 (2018): 077504.

Li, Zhu-bai, Yun Li, Zhi-xin Zhang, Yan-li Liu, Yong-feng Li, and Xue-feng Zhang. "Improving magnetic properties in mischmetal-based sintered composite magnets by regulating element distribution." *AIP Advances* 9, no. 7 (2019).

"Iowa State University Department of Materials Science and Engineering," https://www.mse.iastate.edu/research/microscopy/what-is-the-sem/.

"nanoScience Instruments," https://www.nanoscience.com/techniques/scanning-electron-microscopy/.

A. Nanakoudis, "ThermoFisher Scientific," 2019. https://www.thermofisher.com/blog/materials/edx-analysis-with-sem-how-does-it-work/.

Sasaki, T. T., T. Ohkubo, Y. Takada, T. Sato, A. Kato, Y. Kaneko, and K. Hono. "Formation of non-ferromagnetic grain boundary phase in a Ga-doped Nd-rich Nd–Fe–B sintered magnet." *Scripta Materialia* 113 (2016): 218-221.